Buoyancy transfer across a diffusive interface

By HARINDRA J. S. FERNANDO

Department of Mechanical and Aerospace Engineering, Arizona State University, Tempe,
AZ 85287-6106, USA

An experimental investigation of various aspects of buoyancy transfer across a diffusive density interface that separates stably stratified, turbulently convecting layers of relatively fresh cold water overlying hot salty water is described. It is argued that the interfacial layer should possess a double boundary-layer structure, in which the thicknesses of the salt and heat interfacial layers are determined by a balance between the opposing effects of diffusion and entrainment. Based on this argument, a simple theory, that predicts the interfacial-layer thicknesses, the diffusive heat and salt fluxes across the density interface, and the time variation of the temperature and salt concentrations in the convecting layers, is proposed for the case in which the convection is driven by a constant heat flux supplied to the lower layer. During a certain time interval, the theory and experiment agree well, but thereafter distinct differences can be seen. Measurements suggest that these differences may be due to the distortion of the density interface at low interfacial stabilities by turbulent eddies, which leads to a change in the buoyancy transfer mechanism. When the Richardson number falls below a critical value Ri_v, the interface was found to migrate slowly upwards and the mechanism of entrainment was the detachment of thin sheets of fluid by eddies scouring the interface.

1. Introduction

An understanding of buoyancy transfer across a double-diffusive density interface is important in both geophysical and technological contexts. The nature of such interfaces is dependent upon whether the interface is stable or unstable with respect to the species of high molecular diffusivity. For instance, when the density interface is unstable with respect to a highly diffusive species (e.g. heat) and stable with respect to a species of low diffusivity (e.g. salt), the buoyancy transfer, at high interfacial-layer stabilities, occurs by a purely molecular diffusive mechanism. An interface of this kind is known as a 'diffusive interface'. On the other hand when the interface is stable with respect to a highly diffusive substance and unstable due to a substance of lower diffusivity, long, narrow 'finger-like' convection cells with rising and sinking fluid motions that carry buoyancy flux will be created. These interfaces are known as 'finger interfaces' (Turner 1973, 1974).

Extensive observations have been reported on the existence of a thermohaline staircase structure, consisting of turbulently convecting layers separated by density interfaces, in some areas of the world's oceans. In particular, diffusive interfaces are common in regions where both temperature and salinity increase with depth, such as in polar water masses or lakes with geothermal springs. Some examples are the ice-covered portion of the Arctic ocean (Neal, Neshyba & Denner 1969; Neshyba, Neal & Denner 1971), the Mediterranean outflow into the Atlantic Ocean (Gregg & Cox 1972), Lake Vanda in Antarctica (Shirtcliffe & Calhaem 1968; Hoare 1966, 1968;

Huppert & Turner 1972), Lake Kivu (Newman 1976), Weddell Sea (Foster & Carmack 1976) and the Red Sea (Swallow & Crease 1965; Munns, Stanley & Densmore 1967; Degens & Ross 1969). Besides their geophysical importance, diffusive interfaces are encountered in various engineering flow situations. An example is the diffusive interface formed in solar ponds between the upper cold freshwater layer and the bottom hot salty layer that concentrates the solar energy. The operation of the pond largely depends on the insulating properties of the diffusive interface, which prevents the loss of collected heat from the lower layer. Numerous other applications of double-diffusive convection, for example, in metal solidification and during loading of LNG gas into storage tanks, are discussed in excellent review articles by Turner (1974, 1985) and Huppert & Turner (1981).

Turner & Stommel (1964) were the first to perform laboratory experiments on diffusive interfaces. They demonstrated that, upon heating a stable salinity gradient from below, a series of convecting layers separated by diffusive interfaces are formed. Following this study, Turner (1965) investigated the transfer of heat and salt across a single diffusive interface, formed by heating a two-layer, salt-stratified fluid from below. The experimental results indicated that the ratio of buoyancy fluxes due to salt and heat is a constant, $C \approx 0.15$, viz.

$$R_F = \frac{g\beta F_s}{g\alpha F_h} = C; \quad \text{for } 2 < R_\rho < 7, \tag{1}$$

where F_s and F_h are salt and heat fluxes, α and β are the coefficients of thermal expansion and salinity contraction, g is the gravitational acceleration and R_ρ is the stability parameter, defined in terms of the differences in salinity ΔS and temperature ΔT across the interface, $R_\rho = \beta\Delta S/\alpha\Delta T$. When $R_\rho < 2$, a sudden increase of R_F, which was attributed to turbulent transport, could be observed.† Crapper (1975) performed similar experiments and found general agreement with Turner's results, except that R_ρ for the onset of turbulent transport was found to vary from 1.6 to 4. Shirtcliffe (1973) used sugar and salt solutions to generate a diffusive interface and observed that the ratio of buoyancy fluxes across it equals the square root of the ratio of the sugar and salt diffusivities. On this premise Shirtcliffe (1973) suggested that, for Turner's experiments $C = (k_s/k_h)^{\frac{1}{2}} = \tau^{\frac{1}{2}}$, where k_s and k_h are the molecular diffusivities of salt and heat and τ is the Lewis number. Further, during the experiments with sugar–salt systems, a variable regime could not be identified.

Recent experiments of Takao & Narusawa (1980) did not support Shirtcliffe's (1973) postulate. Their experiments, performed with different solute pairs covering a wide range of τ, revealed a correlation of the form $C = 0.039\tau^{-\frac{1}{3}}$. The experiments of Turner, Shirtcliffe & Brewer (1970) have also been performed using different combinations of solutes and the results support a flux law of the form (see §2.1)

$$R_F = \tau^{\frac{1}{2}}R_\rho. \tag{2}$$

The experiments of Marmorino & Caldwell (1976) and Newell (1984) have covered a wide parameter range. Both of these studies showed general agreement with Turner's results over the same R_ρ range and heat-flux ranges used by Turner (1965). Nevertheless, the former experiments revealed that C is sensitive to the magnitude of the bottom heat flux whereas the latter work shows that, at high R_ρ, the flux law assumes the form

$$R_F = \tau R_\rho. \tag{3}$$

Considerable effort has been applied in the direction of developing theory for the

† Since in this regime R_F is not a constant, it is also called the 'variable regime'.

diffusive buoyancy transfer problem. Huppert (1971) has analysed the stability of a series of diffusive interfaces using an empirical flux law based on Turner's (1965) measurements. When $R_\rho < 2$, the series of layers was shown to be unstable. Linden (1974) used relation (1) together with $C = \tau^{\frac{1}{2}}$ and an entrainment law of the form $E \propto Ri^{-\frac{3}{2}}$ (where E is the entrainment coefficient, $Ri = \Delta b l / u_*^2$ is the Richardson number based on the buoyancy jump Δb across the interface, and the r.m.s. velocity u_*, and the integral length-scale l of turbulence just below the density interface) to predict the R_F vs. R_ρ behaviour of Turner's experiments. Linden's formulation included the scaling argument $g\alpha F_h \sim g\alpha(\overline{T'^2})^{\frac{1}{2}}u_*$, where $(\overline{T'^2})^{\frac{1}{2}}$ is the r.m.s. temperature fluctuation in the interface, and the assumption that the Richardson number based on ΔT, $Ri_T = g\alpha\Delta T l / u_*^2$, is constant over the entire R_ρ range investigated by Turner (1965).

As will be further discussed in §3, a mechanistic model for the buoyancy transfer across diffusive interfaces, that predicts $R_F = \tau^{\frac{1}{2}}$, has been proposed by Linden & Shirtcliffe (1978). This model has been extended by Griffiths (1979) to the multicomponent case and has been further modified by Narusawa (1986). Stern (1982) has reported an investigation on heat and salt transfer across a diffusive interface, using variational methods. The results show that $R_F = \tau^{\frac{1}{2}}$ gives only a lower bound for the flux ratio.

In this paper the results of a study performed on the characteristics of diffusive interfaces are reported. The present work differs from previous investigations in several ways. First, the effect of finite depths of the convecting layers and the time-dependent nature of the buoyancy transfer process are explicitly considered. In addition, the nature of the buoyancy transfer at low R_ρ is investigated in detail. The results of the present study should be helpful in gaining a fundamental understanding of the mixing processes occurring at diffusive interfaces and in modelling phenomena involving diffusive interfaces.

2. A model for the buoyancy transfer

Consider a two-fluid system, which consists of a fresh-water layer of thickness d_u overlying a layer of saline water of thickness d_1. The system is subjected to bottom heating with a constant buoyancy flux q_0, as in figure 1. Here q_0 is defined as

$$q_0 = \frac{g\alpha Q}{\rho_0 C_p}, \tag{4}$$

where ρ_0 is a reference density, Q is the heat flux and C_p is the specific heat at constant pressure. During heating, convective motions are set up first in the bottom layer and then in the top layer. In practice, convection in the upper layer occurs when the thermal boundary layer that develops above the density interface becomes unstable, but the corresponding time delay is neglected and only fluid motions at large times are considered.

2.1. *Thickness of the diffusive interface*

During the convection, salt and heat interfacial layers develop at the density discontinuity. Their equilibrium thicknesses are determined by a balance between the thickening due to diffusion and the entrainment due to convective motions. The upper and lower convective motions have timescales $t_u \sim l_u/u_u$ and $t_1 \sim l_1/u_1$, where u and l represent the velocity and integral lengthscale of convective turbulence and subscripts u and l identify the upper and lower layers. The convective timescale is
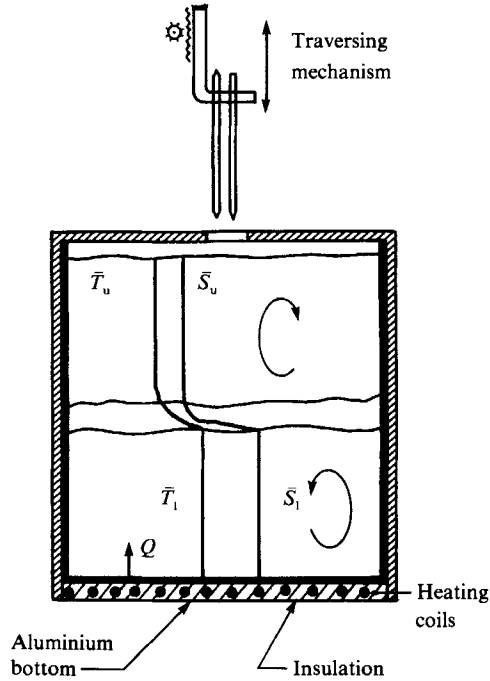
FIGURE 1. A schematic diagram of the experimental set-up showing heating of a two-layer salinity-stratified fluid from below.

representative of the time elapsed between successive entrainment events, caused by the scouring of interfacial-layer fluid by the overturning eddies. Hence, the equilibrium interfacial-layer thicknesses of heat and salt, δ_h and δ_s, can be written as†

$$\delta_h \sim \left(k_h \frac{l_u}{u_u}\right)^{\frac{1}{2}}, \quad \delta_s \sim \left(k_s \frac{l_u}{u_u}\right)^{\frac{1}{2}}. \qquad (5a, b)$$

This approach is similar to that used by Hunt (1983) in estimating the thickness of the diffusive layer that forms during the gas transfer across a liquid–gas interface and physically means that δ_h and δ_s are determined by the extent of the growth of the heat and salt diffusive boundary layers during an eddy turnover event. The corresponding diffusion velocities V_h and V_s can be written as

$$V_h = \frac{k_h}{\delta_h} \sim \left(\frac{k_h u_u}{l_u}\right)^{\frac{1}{2}}, \quad V_s \sim \left(\frac{k_s u_u}{l_u}\right)^{\frac{1}{2}}, \qquad (6a, b)$$

and hence

$$g\beta\Delta S V_s \sim g\beta F_s = A_1 g\beta\Delta S \left(\frac{k_s u_u}{l_u}\right)^{\frac{1}{2}}, \qquad (7a)$$

$$g\alpha\Delta T V_h \sim g\alpha F_h = A_1 g\alpha\Delta T \left(\frac{k_h u_u}{l_u}\right)^{\frac{1}{2}}, \qquad (7b)$$

† The contribution of the turbulent eddies of the lower layer to δ_s and δ_h are of order $(k_s l_1/u_1)^{\frac{1}{2}}$ and $(k_h l_1/u_1)^{\frac{1}{2}}$ respectively. Since $u_u \ll u_1$, the contributions from these quantities are assumed to be negligible.
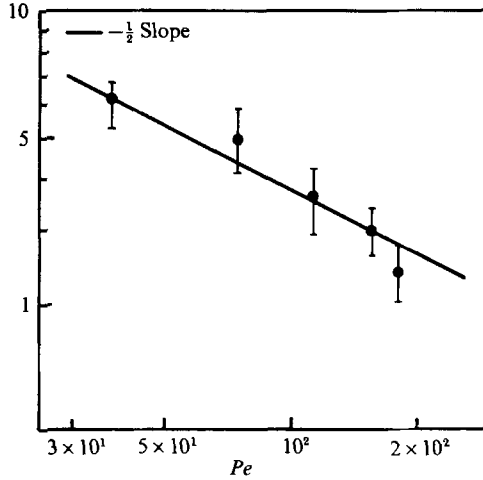
FIGURE 2. Variation of non-dimensional diffusive interfacial-layer thickness with Péclet number (from Crapper & Linden 1974).

where henceforth $A_1, A_2 \ldots$ are used to denote constants. From $7(a, b)$

$$R_F = \frac{g\beta F_s}{g\alpha F_h} = \frac{V_s}{V_h} \frac{g\beta\Delta S}{g\alpha\Delta T} = \tau^{\frac{1}{2}}\left(\frac{\beta\Delta S}{\alpha\Delta T}\right). \tag{8}$$

Note the following:

(*a*) Equation (8) agrees well with the experimental results of Turner *et al.* (1970), the lower limit for R_F of Stern (1982) and the results of Veronis (1968) in the limit $R_\rho \to 1$. According to Veronis (1968), Dr Claes Rooth has offered an explanation for (8) by assuming that initially sharp temperature and salinity interfaces will grow to layers of thicknesses proportional to $k_h^{\frac{1}{2}}$ and $k_s^{\frac{1}{2}}$, before they are swept away by large-scale convecting motions in the layers. This formulation yields $\delta_s/\delta_h = \tau^{\frac{1}{2}}$ and hence (8), provided that the overall ΔS and ΔT across the convecting layers are the same as those across the interface (Turner 1973).

(*b*) Some support for $5(a, b)$ is provided by the experiments of Crapper & Linden (1974), who measured the properties of a heat-stratified diffusive interface surrounded by oscillating grid-induced turbulent layers. The stirring was symmetric. According to (5*a*), the diffusive interfacial-layer thickness should be

$$\frac{\delta_h}{l} \sim \left(\frac{k_h}{ul}\right)^{\frac{1}{2}} = Pe^{-\frac{1}{2}}, \tag{9}$$

where $Pe = ul/k_h$ is the Péclet number based on the r.m.s. velocity u and the integral lengthscale l near the interface. Figure 2 shows δ_h/l *vs.* Pe as plotted from the data of Crapper & Linden (1974). The agreement is satisfactory.

(*c*) $\delta_s/\delta_h = \tau^{\frac{1}{2}}(\ll 1)$ indicates that the interface has a double boundary-layer structure in which the salt interfacial layer is thinner than the heat interfacial layer. To some extent, this result is supported by the measurements of Marmorino & Caldwell (1976), who observed that the salt interface is thinner than the heat interface.

(*d*) It is not clear whether (8) can be directly compared with the experimental results of Turner (1965) and Crapper (1975), whose measurements have been made with a certain amount of mechanical agitation of the layers which, if strong,

introduces an additional velocity scale into the heat and mass transfer process. Further, Turner (1965) and Crapper (1975) assumed steady buoyancy transfer and averaged the fluxes over a suitable period of time. In the present study a determination of the fluxes by taking into account their time-dependent nature was attempted.

2.2. *Estimation of* u_{u}

Using 7 (a, b), the net destabilizing buoyancy flux, $q_T = g\alpha F_{\mathrm{h}} - g\beta F_{\mathrm{s}}$, transferred to the upper layer, becomes

$$q_T = A_1 g\alpha\Delta T \left(\frac{k_{\mathrm{h}} u_{\mathrm{u}}}{l_{\mathrm{u}}}\right)^{\frac{1}{2}} [1 - R_\rho \tau^{\frac{1}{2}}]. \tag{10}$$

Since the upper convecting layer is fully turbulent, on dimensional grounds, it is possible to write†

$$u_{\mathrm{u}} = u_{\mathrm{u}}[q_T, d_{\mathrm{u}}] = A_2 (q_T d_{\mathrm{u}})^{\frac{1}{3}}. \tag{11}$$

Using (10) and (11) and letting $l_{\mathrm{u}} = \gamma_1 d_{\mathrm{u}}$, where γ_1 is a constant (Hunt 1984), the result is

$$u_{\mathrm{u}} = A_3 (g\alpha\Delta T)^{\frac{2}{5}} (k_{\mathrm{h}} d_{\mathrm{u}})^{\frac{1}{5}} [1 - R_\rho \tau^{\frac{1}{2}}]^{\frac{2}{5}}, \tag{12a}$$

and

$$g\alpha F_{\mathrm{h}} = A_4 [(g\alpha\Delta T)^6 k_{\mathrm{h}}^3 / d_{\mathrm{u}}^2]^{\frac{1}{5}} [1 - R_\rho \tau^{\frac{1}{2}}]^{\frac{1}{5}}, \tag{12b}$$

where $A_3 = (A_2^6 A_1^2 / \gamma_1)^{\frac{1}{5}}$ and $A_4 = (A_1^2 A_3 / \gamma_1)^{\frac{1}{2}}$. Note that, according to the proposed mechanism, buoyancy transport is possible only when $R_\rho \tau^{\frac{1}{2}} < 1$. Newell (1984) has observed that the buoyancy transport can take place even when $R_\rho \tau^{\frac{1}{2}} > 1$. However, under such conditions $\delta_{\mathrm{s}} \approx \delta_{\mathrm{h}}$, which indicates the existence of a different transport mechanism.

2.3. *Conservation equations for heat and salt*

The buoyancy conservation equation takes the form

$$\frac{\partial \bar{b}}{\partial t} = \frac{\partial q_b}{\partial z}, \tag{13}$$

where $\bar{b}$ is the mean buoyancy, q_b is the flux of buoyancy, t is the time and z is the vertical coordinate. Assuming the homogeneity of the convecting layers, (13) can be integrated over the lower layer $(0 \leqslant z \leqslant d_1)$ and the upper layer $(d_1 \leqslant z \leqslant d_1 + d_{\mathrm{u}})$ for the salt component, to give

$$g\beta F_{\mathrm{s}} = d_{\mathrm{u}} \frac{\mathrm{d}}{\mathrm{d}t} (g\beta \bar{S}_{\mathrm{u}}), \tag{14}$$

$$g\beta F_{\mathrm{s}} = -d_1 \frac{\mathrm{d}}{\mathrm{d}t} (g\beta \bar{S}_l), \tag{15}$$

where $\bar{S}$ represents the mean salt concentration and the size of the interfacial layers is neglected in comparison with d_{u} and d_1. Similarly, for the heat component, the result is

$$g\alpha F_{\mathrm{h}} = d_{\mathrm{u}} \frac{\mathrm{d}}{\mathrm{d}t} (g\alpha \bar{T}_{\mathrm{u}}), \tag{16}$$

and

$$-g\alpha F_{\mathrm{h}} + q_0 = d_1 \frac{\mathrm{d}}{\mathrm{d}t} (g\alpha \bar{T}_l). \tag{17}$$

† Here it is assumed that the convection in the upper layer is driven by the destabilizing buoyancy flux q_T through the diffusive interface. q_T, in turn, depends on quantities such as k_{s}, k_{h}, $g\alpha\Delta T$, $g\beta\Delta S$ ....

Equations (14)–(17) lead to the total heat and salt conservation equations, viz.

$$g\beta \frac{F_s}{d_*} = -\frac{d}{dt}(g\beta\Delta S), \tag{18}$$

and

$$\frac{q_0}{d_1} - g\alpha \frac{F_h}{d_*} = \frac{d}{dt}(g\alpha\Delta T), \tag{19}$$

where $1/d_* = 1/d_1 + 1/d_u$.

2.4. *Final equations*

From (8), (12b), (18) and (19), it is easy to derive

$$\frac{d}{dt}(g\beta\Delta S) = -\frac{A_4}{d_*}(g\beta\Delta S)(\alpha g\Delta T)^{\frac{1}{3}}\left(\frac{k_s^5 k_h}{d_u^4}\right)^{\frac{1}{10}}[1 - R_\rho \tau^{\frac{1}{2}}]^{\frac{1}{3}}, \tag{20}$$

and

$$\frac{d}{dt}(g\alpha\Delta T) = \frac{q_0}{d_1} - \frac{A_4}{d_*}(\alpha g\Delta T)^{\frac{4}{3}}\left(\frac{k_h^5 k_h}{d_u^4}\right)^{\frac{1}{10}}[1 - R_\rho \tau^{\frac{1}{2}}]^{\frac{1}{3}}. \tag{21}$$

If non-dimensional variables are defined by

$$y = \frac{\alpha g\Delta T}{d_*^{\frac{5}{6}}\left(\frac{d_u^2}{k_h^3}\right)^{\frac{1}{6}}\left(\frac{q_0}{d_1}\right)^{\frac{5}{6}}}, \tag{22a}$$

$$t' = \frac{t}{\left(\frac{d_*^5 d_u^2 d_1}{k_h^3 q_0}\right)^{\frac{1}{6}}}, \quad x = \frac{g\beta\Delta S}{g\beta\Delta S_0}, \tag{22b, c}$$

where ΔS_0 is the initial salinity difference between the layers, and by assuming that, during the convection, $R_\rho \tau^{\frac{1}{2}} \ll 1$, which is certainly the case at large t, (20) and (21) become

$$\frac{dy}{dt'} = 1 - A_4 y^{\frac{6}{5}}, \tag{23a}$$

$$\frac{dx}{dt'} = -A_4 \tau^{\frac{1}{2}} y^{\frac{1}{5}} x, \tag{23b}$$

with $y = 0, x = 1$ at $t' = 0$. The decoupled equation (23a) has a solution of the form

$$t' = \frac{5}{2A_4^{\frac{5}{6}}}\left\{\frac{1}{6}\ln\frac{(A_4^{\frac{1}{6}}y^{\frac{1}{5}}+1)^3}{(A_4^{\frac{1}{6}}y^{\frac{1}{5}}-1)^3}\frac{(A_4^{\frac{1}{6}}y^{\frac{3}{5}}-1)}{(A_4^{\frac{1}{6}}y^{\frac{3}{5}}+1)} + \frac{1}{\sqrt{3}}\tan^{-1}\frac{\sqrt{3}A_4^{\frac{1}{6}}y^{\frac{1}{5}}}{(A_4^{\frac{1}{6}}y^{\frac{2}{5}}-1)}\right\}. \tag{24}$$

The two equations 23(a, b) were solved using a fourth-order Runge–Kutta method. The results, for the case $A_4 \approx 0.062$, are presented in figure 3. The value of A_4 was selected on the basis of the experimental results presented in §5.

3. Comparison with Linden & Shirtcliffe's model

The mechanistic model proposed by Linden & Shirtcliffe (1978) (hereafter LS) assumes that the buoyancy transport across the diffusive interface occurs through a series of 'quasi-steady' steps so that the properties of convection at any given time are the same as would be observed in a steady state with the flow parameters as
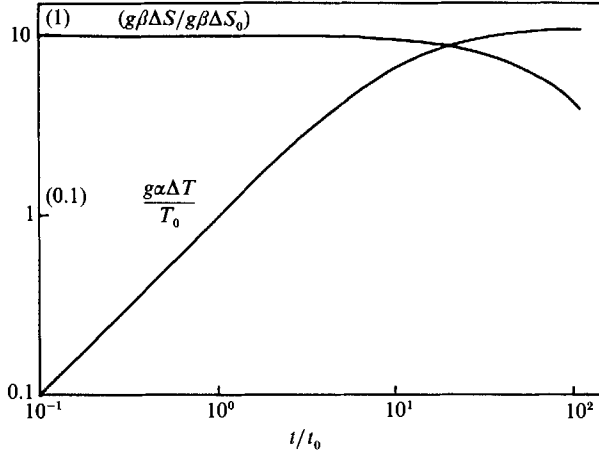
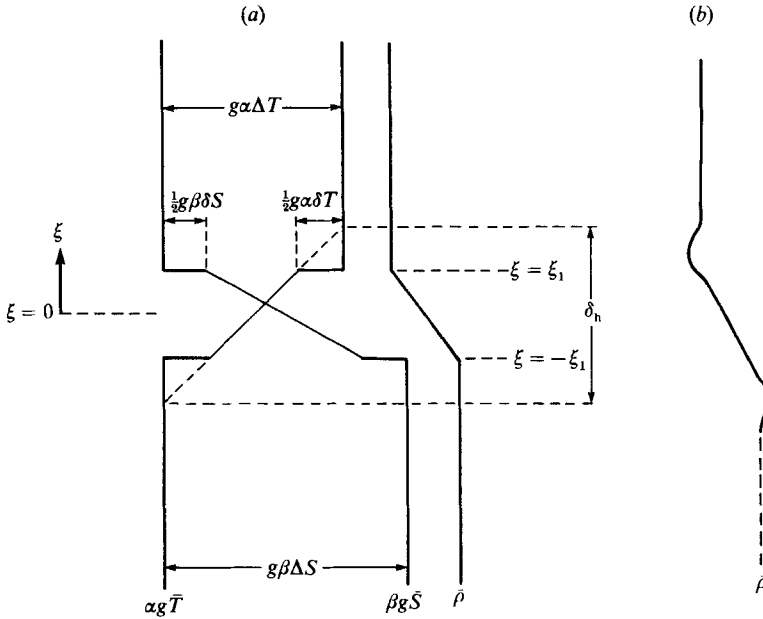FIGURE 3. The numerical solutions for $(23a, b)$ with $A_4 \approx 0.0625$.

FIGURE 4. (a) The temperature, salinity and density $\bar{\rho}$ distribution within and on either side of a diffusive interface, as assumed by Linden & Shirtcliffe (1978). The diffusive core is confined to $-\xi_1 < \xi < \xi_1$. The heat interfacial-layer thickness is denoted by δ_{h}. (b) The density distribution of the system during the growth of the diffusive boundary layers.

observed at that time. The interfacial structure is assumed to consist of three parts, namely a central diffusive core and two unstable boundary layers on either side of it (figure 4a). The analysis was carried out primarily for the case $d_{\mathrm{u}} = d_1 = D$ and $q_0 = 0$. Since, for this case, the $\bar{T}$ and $\bar{S}$ profiles are symmetric about $\xi = 0$, where ξ is the distance measured (upwards) from the centre of the diffusive core, only the upper half of the system $0 \leqslant \xi \leqslant D$ needs to be considered.

Most laboratory studies start with a sharp density interface; it is assumed that the initial transient evolution leads to a repetitive base profile as shown in figure 4 (a). In this configuration the $\bar{S}$ and $\bar{T}$ profiles are linear in the diffusive core and the density

step at the edge of the core $\xi = \xi_1$ is zero owing to the assumption $g\beta\delta S = g\alpha\delta T$, where $g\beta\delta S$ and $g\alpha\delta T$ are the step buoyancy jumps due to salinity and temperature at the edge of the diffusive core. The base profile acts as the initial state $t = 0$ for the subsequent quasi-steady repetitive steps through which the system runs down.

As time proceeds, diffusion causes unstable boundary layers to grow and to form a density inversion just above $\xi = \xi_1$ (figure 4b), which breaks down to release a buoyant 'blob' of fluid (or a thermal) when the thermal Rayleigh number $Ra = \delta b d_T^3/k_h \nu$ of the unstable boundary layer exceeds a critical value Ra_c at a time $t = t_*$. Here ν is the kinematic viscosity, d_T and δb are the characteristic length and buoyancy scales in the unstable boundary layer, defined in terms of the temperature $\bar{T}(\xi, t)$ and salinity $\bar{S}(\xi, t)$ distributions at $t = t_*$ as

$$\delta b \, d_T = \int_{\xi_1}^{\infty} \{g\alpha[\tfrac{1}{2}\Delta T - \bar{T}(\xi, t_*)] - g\beta[\tfrac{1}{2}\Delta S - \bar{S}(\xi, t_*)]\} \, \mathrm{d}\xi \tag{25}$$

and

$$d_T = (\pi k_h t_*)^{\frac{1}{2}} - (\pi k_s t_*)^{\frac{1}{2}}, \tag{26}$$

where $(\pi k_h t_*)^{\frac{1}{2}}$ and $(\pi k_s t_*)^{\frac{1}{2}}$ are the thicknesses of the heat and salt boundary layers above $\xi = \xi_1$. After the buoyant 'blob' leaves, the temperature and salinity profiles revert back to their original forms and the sequence of events repeat. The suitability of the $\bar{S}$ and $\bar{T}$ profiles, immediately after the buoyant element leaves at $t = t_*$, as the initial profiles for the following cycle has been analysed by LS. They showed that, when $\xi_1 \gg 2(k_h t_*)^{\frac{1}{2}}$ and except near $\xi = \xi_1$, the core profiles at $t = t_*$ are approximately the same as the initial profiles and hence the profile shown in figure 4(a) is a satisfactory base profile for the repetitive cycles. The analysis showed that the average heat flux

$$g\alpha F_h = \frac{1}{t_*} \int_{\xi_1}^{\infty} g\alpha(\tfrac{1}{2}\Delta T - \bar{T}(\xi, t_*)) \, \mathrm{d}\xi, \tag{27}$$

and the flux law (§1), can be written in the form

$$g\alpha F_h = \frac{1}{(\pi Ra_c)^{\frac{1}{3}}} \left(\frac{k_h^2}{\nu}\right)^{\frac{1}{3}} (g\alpha\Delta T)^{\frac{4}{3}} \frac{(1 - \tau^{\frac{1}{2}} R_\rho)^{\frac{4}{3}}}{(1 - \tau^{\frac{1}{2}})^{\frac{1}{3}}}, \tag{28}$$

$$\frac{g\beta F_s}{g\alpha F_h} = \tau^{\frac{1}{2}}. \tag{29}$$

The average heat and salt interfacial-layer thicknesses, δ_h and δ_s, defined in terms of the core gradients, $\bar{T}_\xi = \partial\bar{T}/\partial\xi$ and $\bar{S}_\xi = \partial\bar{S}/\partial\xi$, become

$$\delta_h = \frac{\Delta T}{\bar{T}_\xi} = (\pi Ra_c)^{\frac{1}{3}}(k_h^2 \nu)^{\frac{1}{4}} \frac{(1 - \tau^{\frac{1}{2}})^{\frac{1}{4}}}{(1 - \tau^{\frac{1}{2}} R_\rho)} (g\alpha F_h)^{-\frac{1}{4}}, \tag{30a}$$

$$\delta_h = (\pi Ra_c)^{\frac{1}{3}}(\nu k_h)^{\frac{1}{3}} \frac{(1 - \tau^{\frac{1}{2}})^{\frac{1}{3}}}{(1 - \tau^{\frac{1}{2}} R_\rho)^{\frac{4}{3}}} (g\alpha\Delta T)^{-\frac{1}{3}} \tag{30b}$$

$$\equiv P_1$$

and

$$\delta_s = \Delta S/\bar{S}_\xi = \tau^{\frac{1}{2}} R_\rho \, \delta_T. \tag{31}$$

The buoyancy transport mechanism described in §2 differs from that just described and assumes that the thicknesses of the heat and salt interfacial layers, and hence the buoyancy fluxes, are controlled by turbulent motions in the convecting layers. This notion is corroborated by the recent experimental results of Adrian,

Ferreira & Boberg (1986), which indicate that the thermals do not play a dominant role once turbulence is established in the convective layers. The eroding motions of the eddies modify the flow structure near the interface and shortcircuit the processes that lead to the formation of thermals (§5). The buoyancy transport is assumed to occur through a series of quasi-equilibrium steps, as in LS, and the equilibrium thicknesses of the heat and salt interfaces are assumed to be determined by a balance between thickening due to diffusion and entrainment due to convective motions. Turbulent velocity in the upper convective layer is determined by the buoyancy flux through the interface (equation (11)), which in turn controls δ_s and δ_h.

In contrast to LS, the present work assumes that the $\bar{T}$ and $\bar{S}$ profiles are asymmetric about $\xi = 0$ because of the different turbulence levels across the interface. The timescale of the upper-layer convection d_u/u_u makes the dominant contribution to the interfacial-layer thicknesses and therefore, the solutions for heat and salt transport, (8) and (12), are dependent on d_u, whereas the LS solutions, (28) and (29), do not predict such a dependence.

It should be noted that, in the limit considered by LS, i.e. $d_u \to \infty$, the assumptions leading to the present model are violated so that the predictions are not valid. Given that the other variables are constant, as $d_u \to \infty$, $t_u \to \infty$ and the eroding action of the eddies, which prevents the formation of thermals at the interface, becomes inactive. Thus, in this limit, thermals continue to play a dominant role in the buoyancy transfer and the LS theory is expected to be valid.

It is instructive to obtain expressions for the time dependence of ΔT and ΔS, analogous to (23a, b), based on the flux laws of LS. Using (18), (19), (28) and (29), and introducing the non-dimensional parameters

$$p = \frac{g\alpha\Delta T}{\left(\frac{q_0^3 d_*^3 \nu}{d_1^3 k_h^2}\right)^{\frac{1}{4}}}, \quad q = \frac{g\beta\Delta S}{\left(\frac{d_*^3 q_0^3 \nu}{d_1^3 k_h^2}\right)^{\frac{1}{4}}}, \quad t'' = \frac{t}{\left(\frac{d_*^3 \nu d_1}{q_0 k_h^2}\right)^{\frac{1}{4}}} \qquad (32\,a,\,b,\,c)$$

for $\tau^{\frac{1}{2}} R_\rho \ll 1$ the result is

$$\frac{\mathrm{d}p}{\mathrm{d}t''} = 1 - \frac{1}{(\pi Ra_c)^{\frac{1}{3}}} p^{\frac{4}{3}}, \quad \frac{\mathrm{d}q}{\mathrm{d}t''} = -\frac{1}{(\pi Ra_c)^{\frac{1}{3}}} \tau^{\frac{1}{2}} p^{\frac{4}{3}}, \qquad (33\,a,\,b)$$

with $p = 0$, $q = g\beta\Delta S_0 / (d_*^3 q_0^3 \nu / d_1^3 k_h^2)^{\frac{1}{4}}$ when $t'' = 0$. Note that the scaling variables in this case are different from those of (22). Equation 33(a) has a solution of the form

$$t = \frac{3}{2A_5^{\frac{3}{3}}}\left[\frac{1}{2}\ln\frac{(1+A_5^{\frac{1}{3}}p^{\frac{1}{3}})}{(1-A_5^{\frac{1}{3}}p^{\frac{1}{3}})} - \tan^{-1} A_5^{\frac{1}{3}} p^{\frac{1}{3}}\right], \qquad (34)$$

where $A_5 = (\pi Ra_c)^{-\frac{1}{3}}$. In comparing the solutions based on LS theory with the experiments, $Ra_c = 1629$, as proposed by LS, is used.

4. Experimental method

The experimental apparatus is a 14 in. × 14 in. × 14 in. square tank with its sides and base made of $\frac{1}{2}$ in. Plexiglas and $\frac{1}{4}$ in. aluminium plates respectively. All mating parts are fastened by heat-resistant superadhesive glue to avoid leakage due to thermal expansion and the whole assembly is reinforced using aluminium angles. Except for the area necessary for flow visualization, the sides of the tank were covered with Styrofoam to reduce heat losses. The heat flux was supplied using

heating elements arranged in an array with equal spacings. The input voltage to the heating elements could be varied using a potentiometer and heat fluxes up to $5000 \mathrm{Wm^{-2}}$ were possible. An asbestos sheet (thickness $\frac{1}{4}$ in.) separated the aluminium bottom and the heating elements, thus facilitating even heat distribution. Another layer of heat insulation $1\frac{1}{2}$ in. thick was placed underneath the heating coils. The convection tank was placed inside a steel frame that supports the traverse mechanism which carries the temperatures and salinity probes. The heat flux from the bottom of the tank, for various potentiometer settings, was determined by measuring the temperature rise with time of a given amount of fresh water contained in the tank.

A two-fluid system was prepared by carefully feeding the salt water underneath a layer of freshwater so as to form a thin horizontal sheet. During filling, a certain amount of interfacial mixing was found to be inevitable. Using a siphon arrangement, some of the mixed fluid was removed and the resulting fluid system contained only a relatively thin interfacial layer of about 0.5 cm average thickness. Measurements of salinity were made using a single-point conductivity probe and a temperature-compensated refractometer (AO model no. 10419); temperature measurements were made using Chromel/Alumel (type K) fast-response thermocouples. The salinity data were converted to density $\bar{\rho}$ by comparing them with $(\bar{\rho}, \bar{S}, \bar{T})$ calibration curves, experimentally obtained for the entire range of salinity and temperature used in the experiments. For this purpose, the densities of different solutions of different salinities were determined at various temperatures and linear interpolation was used to obtain intermediate values. However, when calculating the variables y, p, t' and t'', α and k_h corresponding to the average temperature of the particular experiment were used.

The vertical temperature and salinity profiles were measured using thermocouples and conductivity probes, mounted on a vertically traversing platform. The output from the thermocouple was connected to a TAC 80K linearizer and an Omni-Amp amplifier. The resulting signal, together with the signals from the conductivity gauge and the voltage divider of the traversing mechanism (which provides a signal proportional to the position of the probes) were fed to a data-acquisition system and two x–y recorders. The interfacial-layer thicknesses were measured by using a technique similar to that used by Crapper & Linden (1974); a straight line was fitted to the mid 50% of the depth–temperature and depth–salinity profiles and the distance between the intersection points of this line and the concentrations corresponding to the upper and lower mixed layers was considered to be the interfacial-layer thickness.

The r.m.s. fluctuations of salinity and temperature in the interfacial layer, $(\overline{S'^2})^{\frac{1}{2}}$ and $(\overline{T'^2})^{\frac{1}{2}}$, were calculated using the time traces of salinity and temperature data registered by conductivity and temperature probes placed in the interfacial layer. The point of measurement was chosen by traversing the conductivity and temperature probe assemblies through the interface and by determining the mid-point of the salt interfacial layer using the salinity/depth profile. The salt and temperature probes were separated horizontally by about 0.5 mm and the time-series records of conductivity and temperature fluctuations could be used to calculate the correlation coefficient $\overline{S'T'}/(\overline{S'^2})^{\frac{1}{2}}(\overline{T'^2})^{\frac{1}{2}}$ between them. The sample of time used in calculating the r.m.s. quantities was limited to 30 s. By assuming that the timescale for the variation of temperature and salinity in the convecting layers is *much higher* than this time period, the r.m.s. fluctuations were calculated by employing the standard techniques available for the stationary processes.

During the experiment, the interfacial position was monitored with a shadowgraph. Owing to the pronounced activity of the eddies impinging on the density interface, the lower boundary of the interfacial layer was quite discernible. After some time, entrainment causes the density interface to rise very slowly, and, by recording the position of the interface at every 50 s, it was possible to estimate the time at which the interface starts migrating. Although such measurements have a certain amount of subjectivity, the distinct flat nature of the lower boundary (§5) and the absence of wave breaking minimize the error incurred in estimating the position of the lower edge.

At the beginning of the experiments, the depths of the upper and lower layers, their salinities and temperatures were recorded. The heat flux was initiated by setting the potentiometer to the desired value. The time count was started when a thermocouple attached to the bottom end of the tank showed a 0.5 °C increase in temperature. The temperatures and the salinities of the convecting layers were measured by appropriate probes placed at the mid-depths of the fluid layers. Further, the salinity data were checked by taking 2 ml samples from the mid-depth of the layers and analysing them using a refractometer. At the beginning of the experiments, $g\alpha\Delta T = 0$, and hence $R_\rho \to \infty$, but, as time proceeds, R_ρ decreases rapidly and convection in the upper layer sets in. The lowest value of R_ρ achieved was 1.7. The temperature–time and salinity–time data were curve-fitted using cubic splines and the curves were differentiated to calculate the heat and salt fluxes using (14) and (16). However, owing to the very slow variations of salinity in the upper layer during the diffusive regime, large time steps were needed for a significant change in salinity, which in turn introduced errors in differentiation. Hence, although the heat flux was measured over the entire experiment, the salt flux was measured only during the 'low-stability' regime† in which the time variation of $\bar{S}_u$ is high.

The errors in measuring ΔT, ΔS and time were estimated to be ± 0.2 °C, $\pm 1\%$ and ± 1 s. Further, the uncertainties of measurements for δ_s and δ_h are expected to be $\pm 10\%$, and $(\overline{T'^2})^{\frac{1}{2}}$ and $(\overline{S'^2})^{\frac{1}{2}}$ to be $\pm 5\%$. Owing to the errors introduced in differentiating $\bar{S}$, $\bar{T}$, $vs.$ t data, an uncertainty of about $\pm 20\%$ is anticipated for the flux measurements.

5. Qualitative observations

Once the heat flux is turned on, thermal plumes rise from the heating surface, impinge on the density interface and spread laterally. Combined shadowgraph observations and profile measurements clearly showed the thickening of the heat interfacial layer and its breakdown to initiate convection in the upper layer; the intensity of the motions in the upper layer seemed to be much lower than that of the bottom layer. The lower edge of the interfacial layer appeared to be sharp while the upper edge was more diffused. The continuous eroding action of strong convective motions in the lower layer seems to be the cause of this effect (figure 5).

Figure 6 is a close-up shadowgraph view of the interfacial region that seems to contain at least two dominant layers. The diffusive nature of the interfacial layer is evident from the negligibly small temperature and salinity fluctuations in this region (§6.2), which also indicates the absence of appreciable internal-wave activity. The latter observation is also verified by the shadowgraph observations of figures 6

† As will be discussed in § 6, a sudden increase in heat and salt fluxes was observed when the interfacial stability drops below a certain level. This is referred to as the 'low-stability' regime.
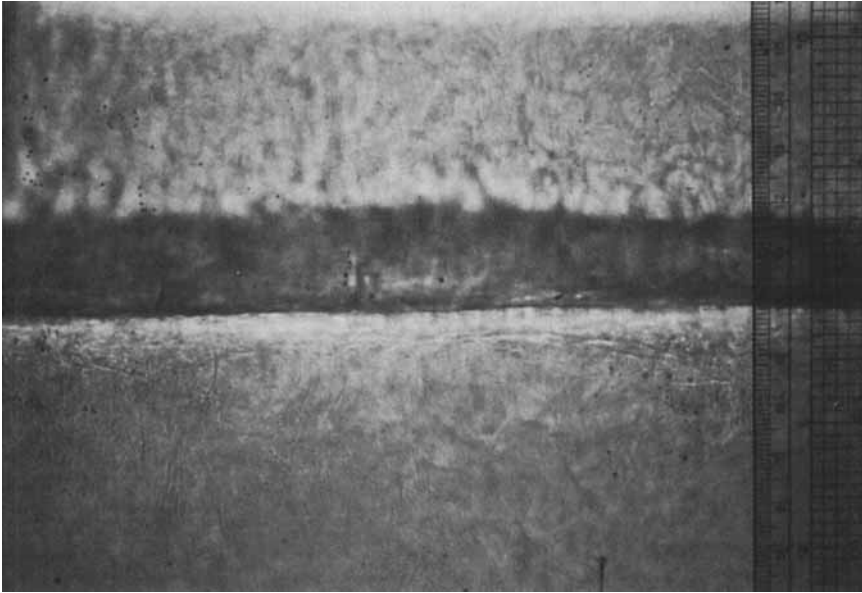
FIGURE 5. A photograph of the interfacial region observed on a shadowgraph when both layers are convecting. Note the sharpness of the lower boundary and the diffused nature of the upper boundary.
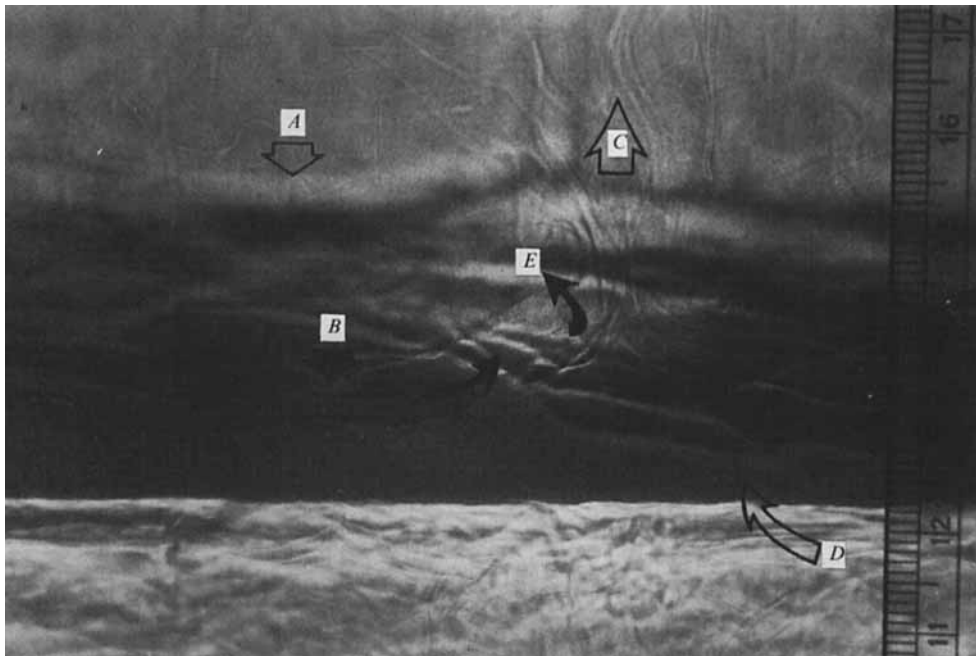

FIGURE 6. A close-up view of the interfacial-layer structure viewed on a shadowgraph. Notice the existence of two distinct layers. A represents the edge of the temperature boundary layer whereas B shows an impression caused by impinging eddies on the salt interfacial layer D. C shows the rising fluid elements conceivably due to scouring of the edge of the salt interface by an eddy. The arrows E are marked to show the possible path of the scouring eddies.

H. J. S. Fernando
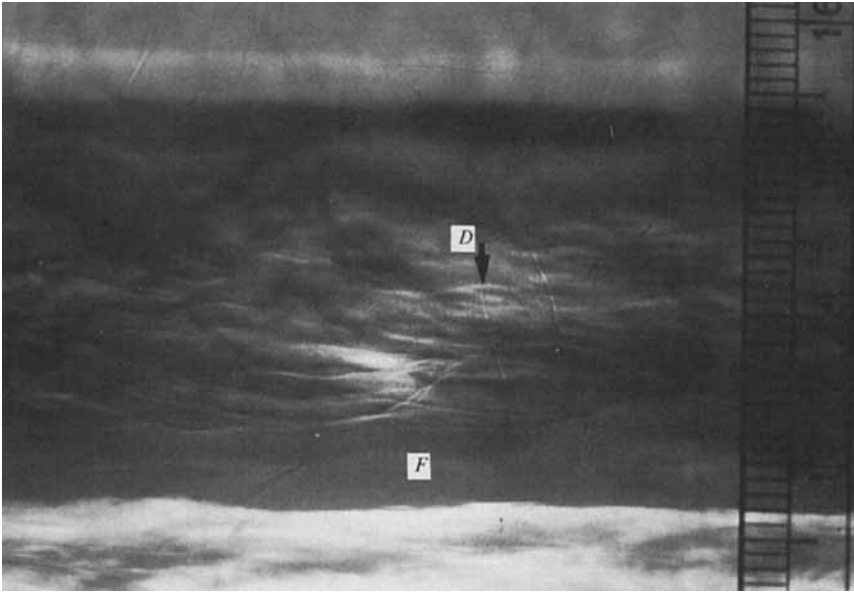
FIGURE 7. A photograph that shows the striations, D, possibly resulting from the impingement of descending eddies on the thermal boundary layer. Owing to the stability of the salt boundary layer these eddies cannot penetrate into the salt boundary layer F and hence the striations cannot be observed within this region.
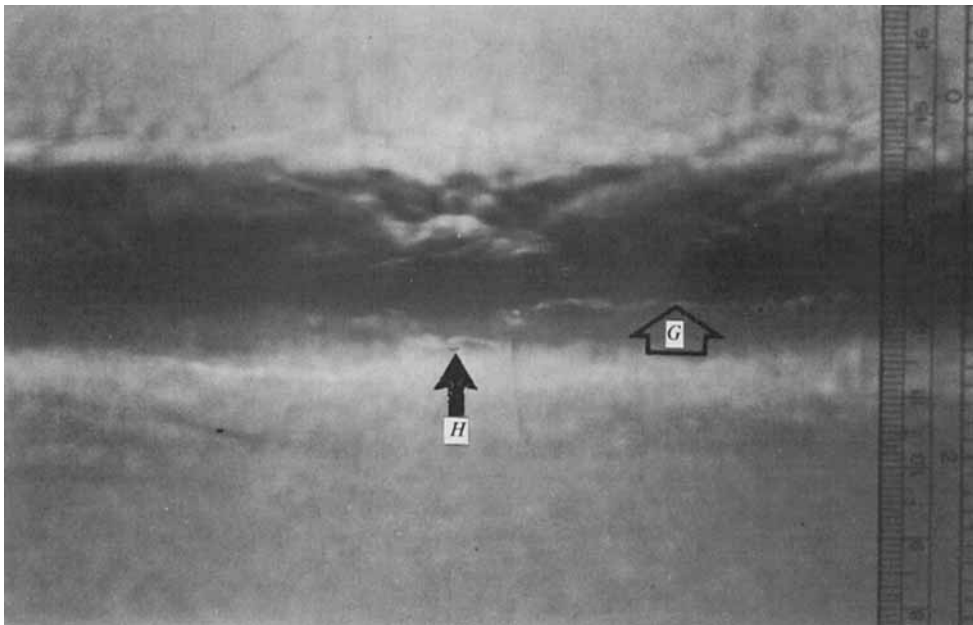
FIGURE 8. Interfacial structure at the verge of initiation of the low-stability regime. Under these conditions, the eddies can penetrate into the stable salt interfacial layer G and distort the interface. H represents the initial location of the base of the salt interfacial layer.
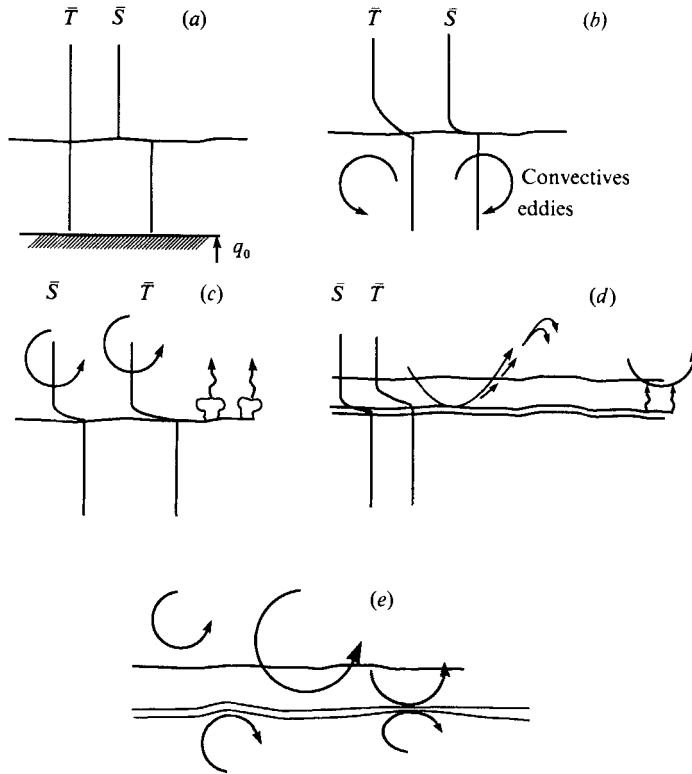
FIGURE 9. Sketches showing a possible sequence of events after the heat flux is turned on.

and 7. The region above the salt interfacial layer is unstably stratified (but not sufficiently unstable to overturn) and is intermittently agitated by turbulent eddies of the upper layer. Apparently, owing to the high stability of the salt boundary layer, the eddies can penetrate only up to its upper edge. This may explain why the 'scars' of the impinging eddies cannot be seen in the lower part of the interface. Owing to heat and salt transfer to the upper layer, the buoyancy jump across the interface decreases gradually and, at a certain interfacial stability, the eddies of the lower, strongly convecting layer start penetrating the salt boundary layer, thus distorting it and increasing the area available for heat and salt transfer (figure 8). At this point, a drastic increase in the heat and salt fluxes, as well as in the r.m.s. temperature and salinity fluctuations within the salt interfacial layer could be observed. During the buoyancy transfer at high interfacial stabilities, $\delta_h > \delta_s$ was observed whereas on the verge of the low-stability regime, a sharp reduction in δ_s and δ_h, in such a way that $\delta_s \approx \delta_h$ could be seen. Interfacial movement under the differential turbulence levels between the upper and lower layers was a prominent feature during the low-stability buoyancy transport regime.

Based on the above observations, the measurements described in §§6 and 7 and the supporting work of other researchers, it is possible to suggest a plausible set of events that could occur during the heating of a two-layer salt-stratified fluid from below. Figure 9(a) shows the initial conditions and figure 9(b) represents the establishment of convection in the lower layer and the development of the thermal and salt boundary layers due to diffusion. The thermal boundary layer then becomes unstable and initiates convection in the upper layer as illustrated in figure 9(c). According to
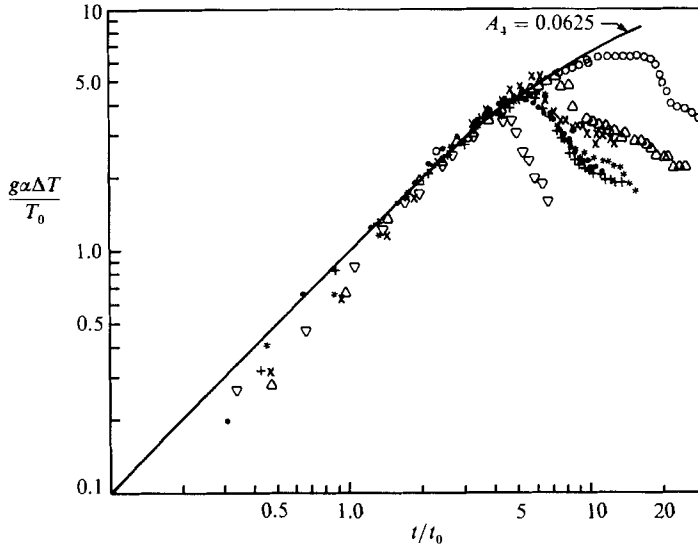
FIGURE 10. Variation of $y = g\alpha\Delta T/T_0$ with $t' = t/t_0$ for seven different experiments. Symbols indicate: $+$, $q_0 = 0.112$ cm^2/s^3, $d_u = 5.334$ cm, $d_1 = 7.62$ cm; $\bullet$, 0.137, 8.2, 7.8; $*$, 0.121, 6, 6; $\times$, 0.114, 5, 7; $\triangle$, 0.099, 4.6, 7.5; $\bigcirc$, 0.070, 4.75, 6.75, $\bigtriangledown$, 0.1558, 7.5, 6. The solid line represents the solution to $(23a)$ with $A_4 \approx 0.062$.

Adrian *et al.* (1986), at the onset, hot fluid elements rise in the form of thermals as described by Sparrow, Husar & Goldstein (1970) but, once the turbulent motion is established in the surrounding fluid, these forms are eroded by the turbulent eddies. Figure 9(*d*) shows that the convective turbulence in the upper layer has been fully established and is driven by the heat flux transferred to the eddies during their contact with the thermal boundary layer. Thus, the heat and salt fluxes are carried to the mixed region by the eddies as a result of their agitation of the interfacial region. Figure 9(*e*) illustrates the formation of interfacial distortions at low interfacial stabilities. These deformations increase the area available for heat transfer as well as the probability for direct physical contact between the eddies of the two layers.

6. Diffusive transport regime

6.1. *Transport of heat and salt*

As mentioned in §4, the time history of the temperatures and salinities of the upper and lower convecting layers were recorded. The non-dimensional quantity $y = g\alpha\Delta T/T_0$, where $T_0 = d_*^{\frac{5}{6}}(d_u^2/k_h^3)^{\frac{1}{6}}(q_0/d_1)^{\frac{5}{6}}$, is plotted as a function of $t' = t/t_0$, where $t_0 = (d_*^5 d_u^2 d_1/k_h^3 q_0)^{\frac{1}{6}}$, in figure 10 for seven different experiments. The solid line depicts the theoretical solution. Perhaps owing to errors introduced by the selection of an arbitrary origin and the validity of (23) only at large t', theory and experiment do not show a good agreement at small t', but starting from $t' \approx 1$, for a certain period of time, the agreement is excellent. At a time $t = t_b$, which depends on the initial stratification and the heating rate, the experimental results tend to deviate from the theory. The temperature difference tends to fall off rapidly and t_0 does not seem to be the proper scaling parameter for t_b. Figure 11 shows the corresponding plot for the salinity variation, i.e. $x = g\beta\Delta S/g\beta\Delta S_0$ *vs.* $t' = t/t_0$. Note that the experimental results follow the same trend as in the previous case. The change in behaviour at
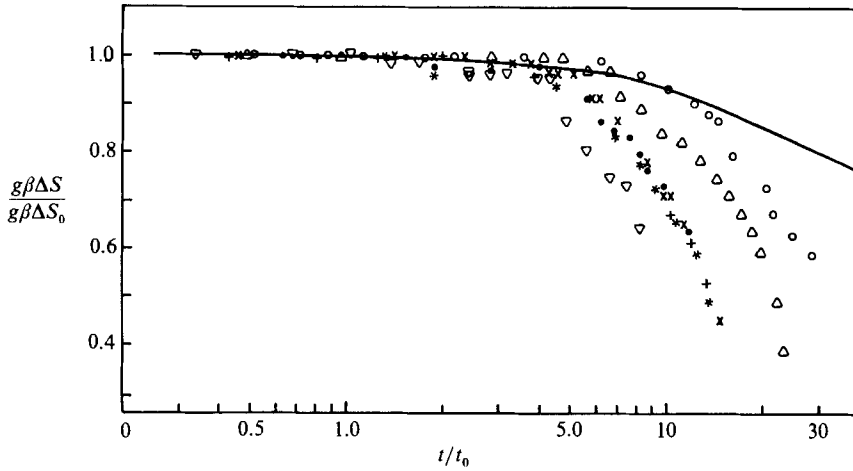
FIGURE 11. Variation of $x = g\beta\Delta S/g\beta\Delta S_0$ with $t' = t/t_0$. The symbols have the same meaning as in figure 10.
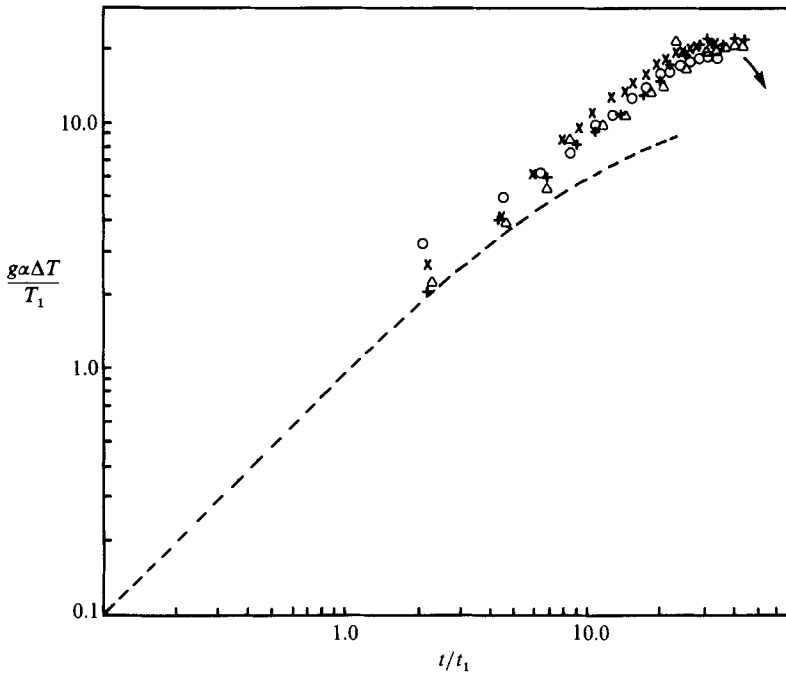

FIGURE 12. Variation of $p = g\alpha\Delta T/T_1$ with $t'' = t/t_1$ for four different experiments. The broken line represents the solution (34).

$t = t_b$ seems to be due to the initiation of a different transport mechanism, which will be addressed in detail in §7. A comparison between the present data and the LS model is depicted in figure 12, as a plot of $p = g\alpha\Delta T/T_1$ vs. $t'' = t/t_1$, where $T_1 = (q_0^3 d_*^3 \nu/d_1^3 k_h^2)^{\frac{1}{4}}$ and $t_1 = (d_*^3 \nu d_1/q_0 k_h^2)^{\frac{1}{4}}$. Only the data up to $t = t_b$ are presented and the broken line represents (34).

Figure 13 shows the variation of the heat flux $g\alpha F_h$ measured during the diffusive transport regime with $[(g\alpha\Delta T)^6 k_h^3/d_u^2]^{\frac{1}{5}}[1 - R_\rho \tau^{\frac{1}{2}}]^{\frac{1}{5}}$. The results seem to be in agreement

H. J. S. Fernando
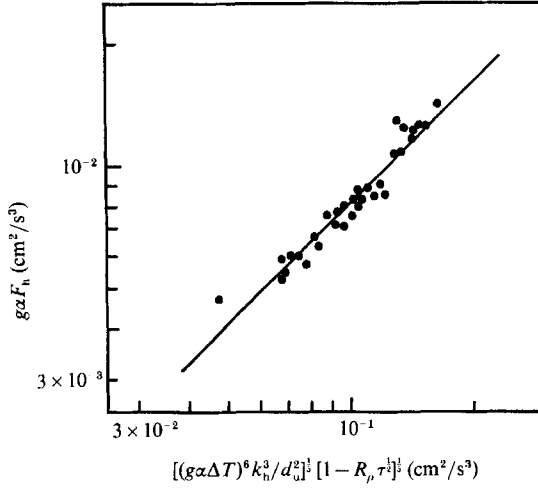
FIGURE 13. Variation of $g\alpha F_h$ with $[(g\alpha\Delta T)^6 k_h^3/d_u^2]^{\frac{1}{5}} [1-R_\rho\tau^{\frac{1}{2}}]^{\frac{1}{5}}$.
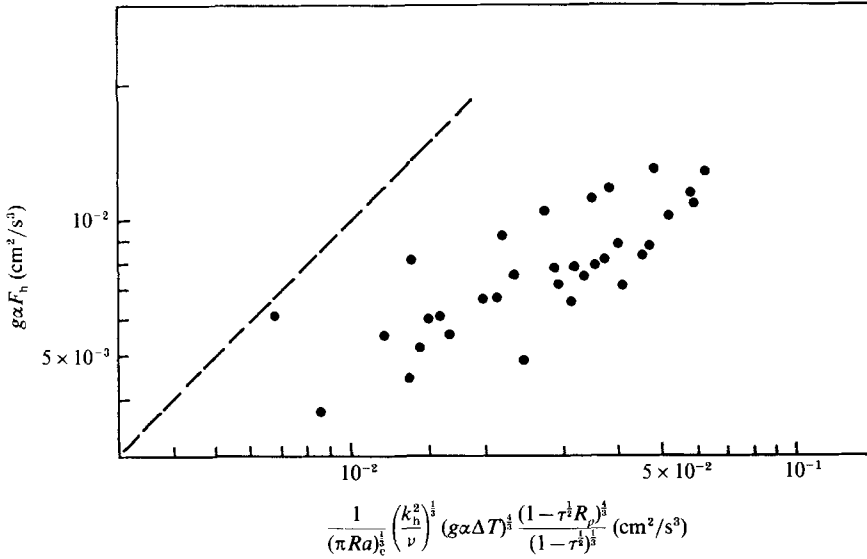
FIGURE 14. Variation of $g\alpha F_h$ with $(k_h^2/\nu)^{\frac{1}{3}} (g\alpha\Delta T)^{\frac{4}{3}} (1-\tau^{\frac{1}{2}}R_\rho)^{\frac{4}{3}}/[\pi Ra_c(1-\tau^{\frac{1}{2}})]^{\frac{1}{3}}$. The broken line indicates the prediction (28).

with (12) with $A_4 \approx 0.075$. If the data are plotted neglecting the $R_\rho\tau^{\frac{1}{2}}$ term, the result is $A_4 \approx 0.068$, which is in agreement with the results of figure 10. Also, using the typical values $\gamma_1 \approx 0.25$ and $A_2 = 1.8^{\frac{1}{2}}$ (Hunt 1984), $A_1 \approx 0.050$ and $A_3 \approx 0.57$. Figure 14 shows a comparison between the present heat-flux measurements and the prediction of the LS theory, as a plot between the left- and right-hand sides of (28). The agreement is not as satisfactory as the case presented in figure 13.

As is evident from (28) and (12b), in the limit of $R_\rho\tau^{\frac{1}{2}} \ll 1$, the LS formulation predicts

$$g\alpha F_h = f_1(g\alpha\Delta T, \nu, k_h), \qquad (35)$$

while in the present work

$$g\alpha F_h = f_2(g\alpha\Delta T, k_h, d_u), \qquad (36)$$
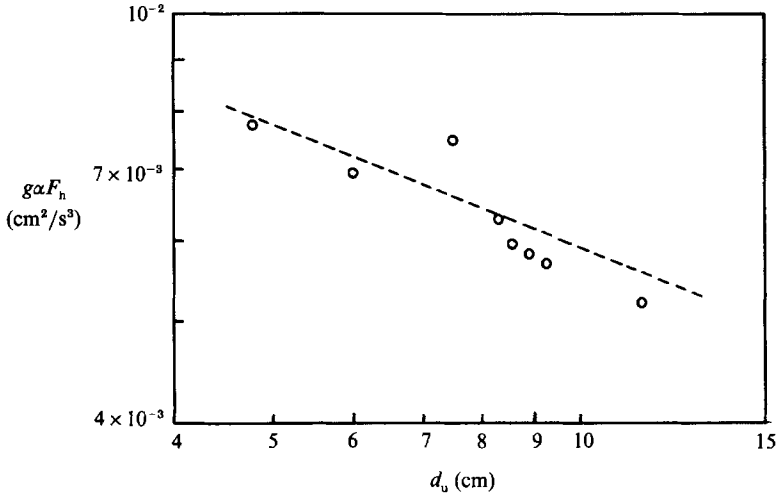
FIGURE 15. A plot of $g\alpha F_h$ vs. d_u, evaluated at constant $g\alpha\Delta T$ (≈ 9.8 cm²/s), k_h and ν. The dotted line has a $-\frac{2}{5}$ slope, corresponding to (12b). During the experiments corresponding to $d_u = 6$, 8.9, 9.2 and 11.5 (cm), R_ρ was also constant (≈ 5.2).
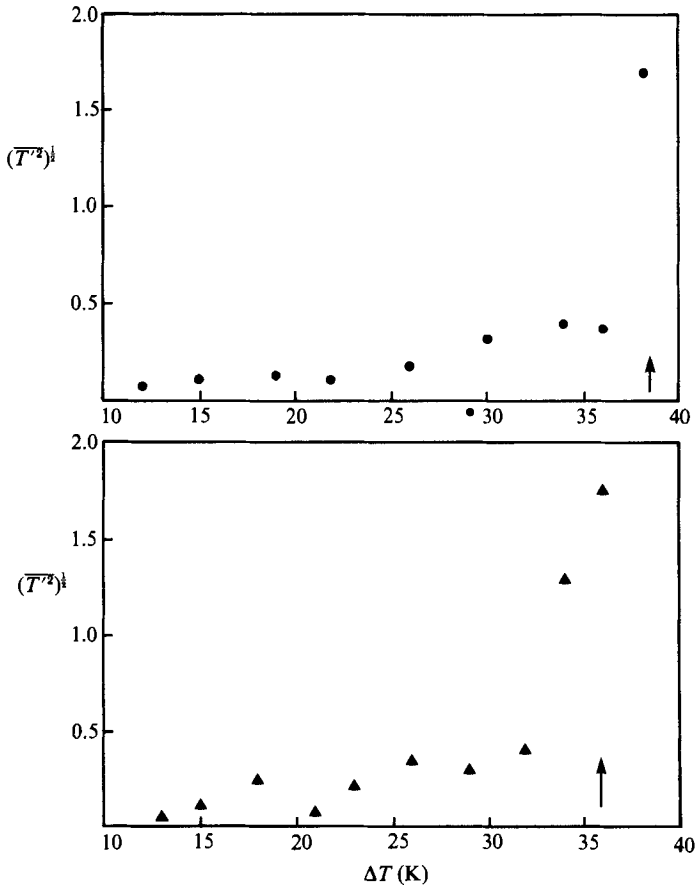

FIGURE 16. A plot of r.m.s. temperature fluctuations $(\overline{T'^2})^{\frac{1}{2}}$, vs. the temperature difference across the interface ΔT.
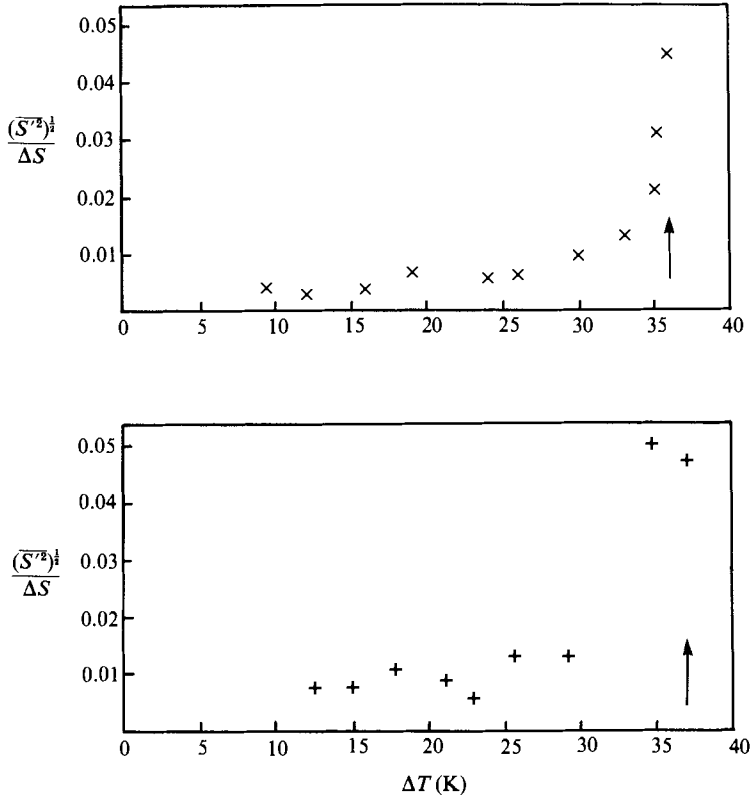
FIGURE 17. A plot of r.m.s. salinity fluctuations $(\overline{S'^2})^{\frac{1}{2}}$, normalized by the salinity difference across the interface ΔS, *vs.* the temperature difference across the interface ΔT.

where f_1 and f_2 are functions. To investigate the possible dependence of $g\alpha F_{\rm h}$ on $d_{\rm u}$, experiments were carried out with varying $d_{\rm u}$ with the heat flux evaluated at a constant $g\alpha\Delta T$. For the temperature range covered in the experiments, $k_{\rm h}$ and ν can be considered as approximately constant. Figure 15 shows a plot of $g\alpha F_{\rm h}$ *vs.* $d_{\rm u}$, evaluated at constant $g\alpha\Delta T$. A clear dependence between the two variables can be discerned, indicating support for (36).

6.2. *Measurement of temperature and salinity fluctuations*

The measurement of the r.m.s. temperature and salinity fluctuations were made within the salinity interfacial layer. The results are depicted in figures 16 and 17. Note that initially the values of $(\overline{S'^2})^{\frac{1}{2}}$ and $(\overline{T'^2})^{\frac{1}{2}}$ are small but, at a certain ΔT, an abrupt increase can be seen. It is interesting that this particular ΔT corresponds to the time at which the experimental results deviate from the theory based on diffusive transport assumptions, and where a sharp increase in heat and salt fluxes could be seen. The qualitative observations described in §5 together with the above observations suggest that the deviation of theory (based on diffusive buoyancy transport assumptions) and experiments may be due to the onset of interfacial distortions.

Figure 18 shows the variation of the correlation coefficient $\overline{S'T'}/(\overline{S'^2})^{\frac{1}{2}}(\overline{T'^2})^{\frac{1}{2}}$ with ΔT. During the diffusive transfer, although the r.m.s. values are small, a high correlation between S' and T' can be seen. This observation suggests that the r.m.s.
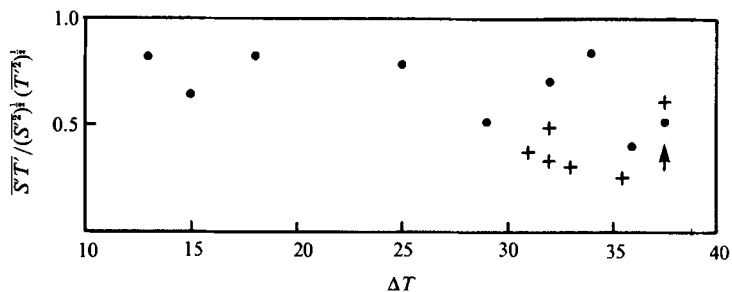
FIGURE 18. Variation of the correlation coefficient between salinity and temperature fluctuations $\overline{S'T'}/(\overline{S'^2})^{\frac{1}{2}}(\overline{T'^2})^{\frac{1}{2}}$ vs. the temperature difference across the interface ΔT. The symbols ● and + represent the data taken during 'diffusive' and 'low stability' buoyancy transfer regimes respectively.

fluctuations may be predominantly associated with small oscillations of the density interface caused by the impinging eddies. It is also seen that the correlation coefficient during the low-stability transport regime is somewhat lower. In this regime the interfacial layer is relatively thin and the eddies continuously penetrate through the interface, thus impinging on each other and with the probe. Apparently, the occurrence of such complicated processes reduces the correlation between T and S within the interface.

6.3. *Measurement of the interfacial-layer thicknesses*

The thicknesses of the salt and heat interfacial layers are a key factor in the determination of the diffusive heat and salt transport. Using (5) and (12a), these thicknesses are evaluated as

$$\delta_{\mathrm{h}} = A_6 \left(\frac{k_{\mathrm{h}}^2 d_{\mathrm{u}}^2}{g \alpha \Delta T} \right)^{\frac{1}{5}} \left(1 - \frac{\beta \Delta S}{\alpha \Delta T} \tau^{\frac{1}{2}} \right)^{-\frac{1}{5}}, \tag{37a}$$

$$\delta_{\mathrm{s}} = A_6 \tau^{\frac{1}{2}} \left(\frac{k_{\mathrm{h}}^2 d_{\mathrm{u}}^2}{g \alpha \Delta T} \right)^{\frac{1}{5}} \left(1 - \frac{\beta \Delta S}{\alpha \Delta T} \tau^{\frac{1}{2}} \right)^{-\frac{1}{5}} \tag{37b}$$

$$= A_6 \tau^{\frac{1}{2}} P.$$

The heat and salt interfacial-layer thicknesses (§4) have been measured using the salinity/temperature–depth profiles obtained during the experiments (figures 19 and 20) and the results are depicted in figures 21 (a, b) and 22. Figure 23 is drawn to compare the present results with the LS model, i.e. equation (30b). Note that the experiments show an increase of δ_{h} with P and predict $A_6 \approx 11$, thus supporting the assumptions made on the formation of the heat boundary layer. Nevertheless, δ_{s} does not seem to be proportional to P, with a proportionality constant of $A_6 \tau^{\frac{1}{2}}$ as predicted by 37 (b). Since the model predictions of buoyancy fluxes appear to be in good agreement with the experimental results (at least over a certain period of time) and since the predictions of the interfacial-layer thicknesses form the basis of the theory, it is instructive to investigate the reasons for such an anomaly and to assess its implications for the predictions of the theory. A possible reason for the observed high value of δ_{s} is the diffused nature of the initial salinity profile. Contrary to the theoretical assumptions, the initial experimental salinity profile does not have a sharp salinity jump and has a finite thickness ranging from 0.2 to 1 cm, depending on ΔS_0 (§4). Let us assume that the experiments were started with a slightly diffused,
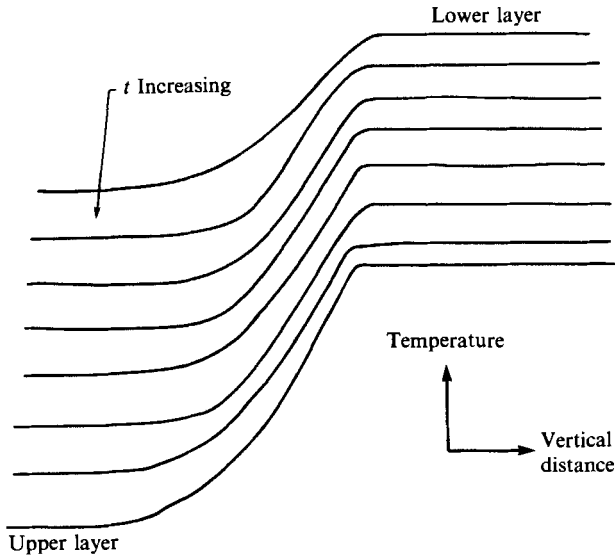
FIGURE 19. A set of raw depth–temperature profiles obtained through the diffusive interface. Note the sharpness of the lower boundary. Scales for the temperature and distance axes are 9.6 K/cm and 1.0 cm probe travel/cm.
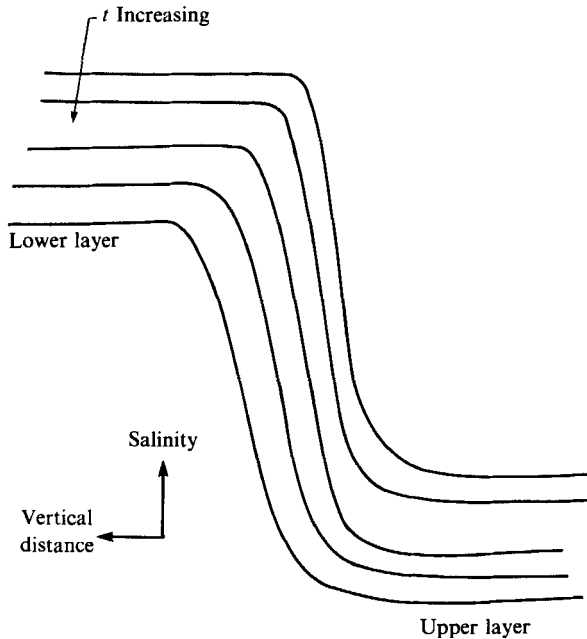

FIGURE 20. A set of raw depth–salinity (conductivity) profiles obtained through the diffusive interface. Scales for the salinity and distance axes are 20%/cm and 2 cm probe travel/cm.

thin interface. Convection in the lower layer starts first and conduction through the interface leads to convection in the upper layer. As long as the initial thickness of the diffused salt interface is smaller than the thickness of the heat interfacial layer, which is formed as a result of convective motions, the diffusive heat transfer can occur as predicted by (12) and (21), in the limit $\tau^{\frac{1}{2}}R_\rho \ll 1$, without being affected by the nature
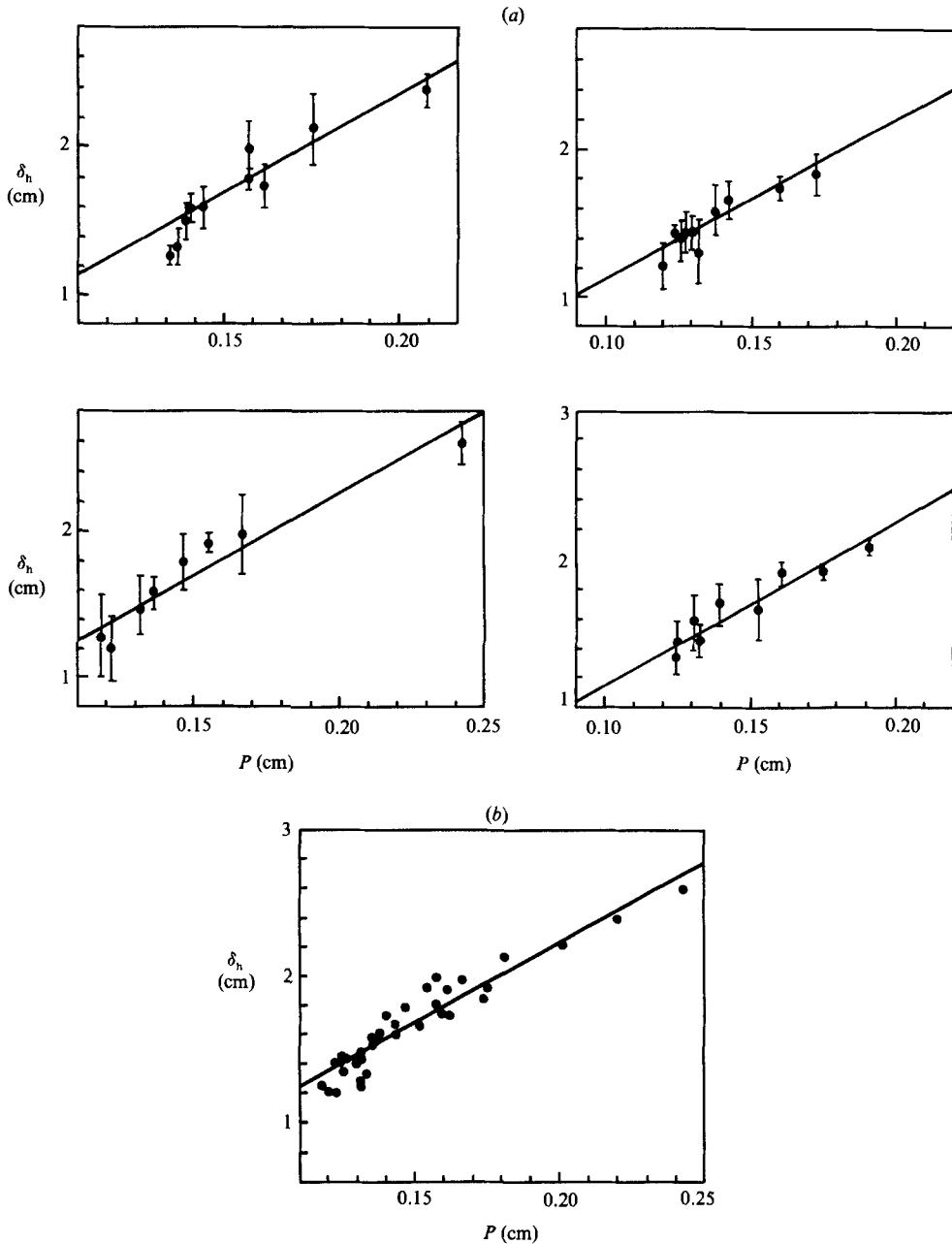
FIGURE 21. (a) Variation of the heat interfacial-layer thickness δ_h vs. P for different experiments. The error bars represent the deviation observed when several instantaneous profiles were used to calculate mean δ_h. (b) All the data of (a) are placed in a single plot.

of the salt interface. However, the salt transport across the interface will be sensitive to the initial interfacial salinity profile, but the corresponding salt flux is so small that, within the accuracy of the experimental techniques employed, it is difficult to detect such deviations from the theoretical predictions. If it is assumed that the (molecular diffusive) growth and entrainment processes of the salt boundary layer
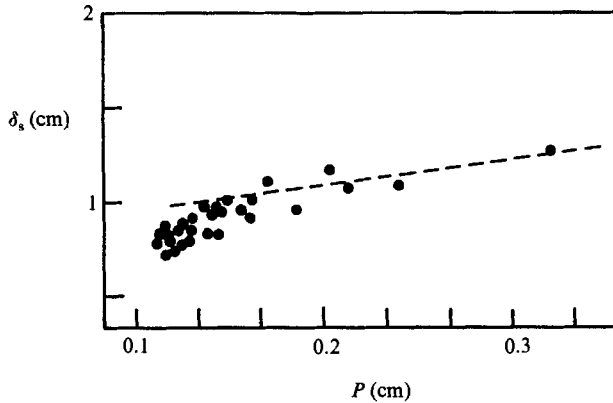
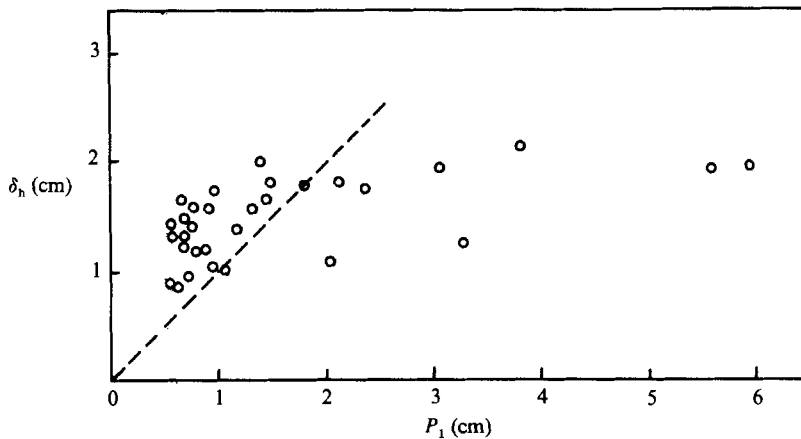FIGURE 22. Variation of the salt interfacial-layer thickness δ_s with P.

FIGURE 23. Variation of heat interfacial-layer thickness δ_h with $P_1 = (\pi Ra_c)^{\frac{1}{3}} (\nu k_h)^{\frac{1}{3}}$ $(1-\tau^{\frac{1}{2}})^{\frac{1}{3}}/(g\alpha\Delta T)^{\frac{1}{3}} (1-\tau^{\frac{1}{2}}R_\rho)^{\frac{4}{3}}$. The broken line represents (30b).

are superimposed on the initial salinity interfacial layer of non-zero thickness, it is possible to expect δ_s to take the form $\delta_s = A_6 \tau^{\frac{1}{2}}P + e$, where the intercept e depends on the initial thickness of the salinity interface, which varies from experiment to experiment. For the purpose of comparison, a straight line with a slope of $A_6 \tau^{\frac{1}{2}}$ ($\tau^{\frac{1}{2}} \approx 0.1$) and an intercept of ≈ 0.90 cm has been drawn on figure 22 by 'eye'.

Measurements of the heat interfacial-layer thickness have been reported previously by Crapper (1975), Marmorino & Caldwell (1976) and Newell (1984). Crapper's experiments show an increasing trend of δ_h with R_ρ in the range $1 < R_\rho < 3$. Since in our experiments, P increases with R_ρ, Crapper's result seems to be in qualitative agreement with ours. Marmorino & Caldwell also report an increase in δ_h with R_ρ; in addition, they find that δ_h is also dependent on the heat input to the lower convecting layer.

7. Heat and salt transport at low interfacial stabilities

7.1. *Onset of low-stability regime*

Thus far, in all experiments performed with heat/salt combinations, an abrupt increase in R_F has been observed at low $\beta\Delta S/\alpha\Delta T$ ratios. As pointed out earlier, in Turner's (1965) experiment, this increase can be seen when $R_\rho \approx 2$ whereas Crapper (1975) reported that this critical $R_\rho(=R_{\rho c})$ is a function of other parameters and can be small as 1.6. Studies of Marmorino & Caldwell (1976) indicate that $R_{\rho c}$ can be much larger than 2. In contrast, such an increase in the flux ratio has not been observed in the experiments performed with sugar and salt solutions (Shirtcliffe 1973).

According to Turner (1965), when $R_\rho < 2$, the observed heat flux is greater than the flux that is expected if the interface is replaced by a perfectly conducting solid plane. This was explained as an effect of the wavy, breaking interface which brings elements with greater temperature contrasts into contact and increases the surface area. Huppert (1971) has offered an alternative explanation assuming that there is a change of boundary conditions, from zero velocity (corresponding to high stabilities) to zero stress (corresponding to low stabilities) at $R_\rho \approx 2$. In our experiments, $R_{\rho c}$ was found to vary from 2 to 4.5 and the measurements suggest that the increase of fluxes may be due to the onset of interfacial distortions by turbulent eddies in the lower layer (§§5 and 6.2).

If the diffusive interface has a double boundary-layer structure, the stable stratification occurs in the overlapping region, stratified with both salt and heat. The buoyancy difference across this layer, of thickness δ_s, can be written as

$$\Delta b_s \approx -\frac{(g\alpha\Delta T)}{(k_h l_u/u_u)^{\frac{1}{2}}}\left(k_s\frac{l_u}{u_u}\right)^{\frac{1}{2}} + g\beta\Delta S, \tag{38a}$$

or
$$\Delta b_s \approx g\beta\Delta S[1 - R_\rho^{-1}\tau^{\frac{1}{2}}]. \tag{38b}$$

If the increase in buoyancy fluxes occurs when the interfacial stability drops to a level where the turbulent eddies of the lower layer are energetic enough to overcome the stratification and penetrate into the interfacial layer, the criterion for the onset of the low-stability regime may be written as

$$g\beta\Delta S[1 - R_\rho^{-1}\tau^{\frac{1}{2}}]\left(\frac{k_s d_u}{u_u}\right)^{\frac{1}{2}} \sim (q_0 d_1)^{\frac{2}{3}}, \tag{39}$$

where the r.m.s. velocity just below the density interface due to convective turbulence can be estimated as $u_*^2 = C_1(q_0 d_1)^{\frac{2}{3}}$, where $C_1, C_2 \ldots$ are constants, $C_1 \approx 1.8$ (Hunt 1984). Using (12a) and (39),

$$R_\rho(g\alpha\Delta T)^{\frac{4}{5}}\left(\frac{k_s^5 d_u^4}{k_h}\right)^{\frac{1}{10}}\frac{[1 - R_\rho^{-1}\tau^{\frac{1}{2}}]}{[1 - R_\rho\tau^{\frac{1}{2}}]^{\frac{1}{5}}} = C_2(q_0 d_1)^{\frac{2}{3}}, \tag{40a}$$

or
$$R = C_2(q_0 d_1)^{\frac{2}{3}}.$$

Equation (40a) also can be written as

$$\frac{x}{y^{\frac{1}{5}}} = C_2\left(\frac{d_1 d_* q_0^5}{d_u^2 k_s^3}\right)^{\frac{1}{5}}\frac{1}{g\beta\Delta S_0}\left[\frac{(1 - R_\rho\tau^{\frac{1}{2}})^{\frac{1}{5}}}{(1 - R_\rho^{-1}\tau^{\frac{1}{2}})}\right]$$

$$= C_2 Q. \tag{40b}$$

Figure 24 shows $xy^{-\frac{1}{5}}$ *vs.* Q at the onset of the low-stability transport, estimated
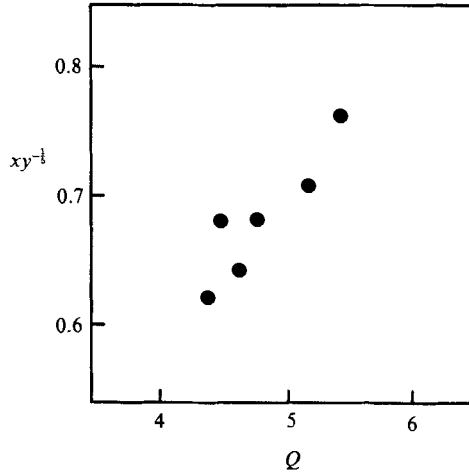
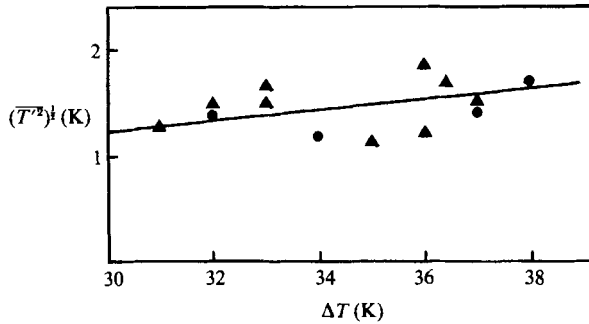FIGURE 24. Estimation of the departure points between the theory and the experiment: A plot of $xy^{-\frac{1}{5}}$ vs. Q.

FIGURE 25. Variation of r.m.s. temperature fluctuations within the salt interfacial layer $(\overline{T'^2})^{\frac{1}{2}}$ with the temperature difference ΔT during the low-stability regime.

from the departure point between the theory and the experimental results of figure 10. The agreement is fair and supports the notion that the observed increase in heat/salt fluxes is due to the initiation of a new buoyancy transfer mechanism. Also the average C_2 was calculated as $C_2 = R/(q_0 d_1)^{\frac{2}{3}} = x/y^{\frac{1}{5}}Q \approx 0.15$.

From the preceding discussion, it is clear why systems other than heat/salt combinations with an imposed heat flux do not show the low-stability transport regime. In such cases, the only driving mechanism for convective motions is the difference in solute concentrations between the layers, which decreases gradually. As a result the convective velocities in the layers also decrease and hence a mechanism of the nature described above cannot operate.

7.2. Measurements of the temperature and salinity fluctuations and the interfacial-layer thicknesses

As is evident from figures 16 and 17, the heat and mass transport at low interfacial stabilities are associated with high values of r.m.s. salinity and temperature fluctuations. The temperature and salinity fluctuations within the interfacial layer during the low-stability regime have been measured. The results are shown in figures 25 and 26. These measurements suggest that $(\overline{S'^2})^{\frac{1}{2}} \propto \Delta S$ and $(\overline{T'^2})^{\frac{1}{2}} \propto \Delta T$, with
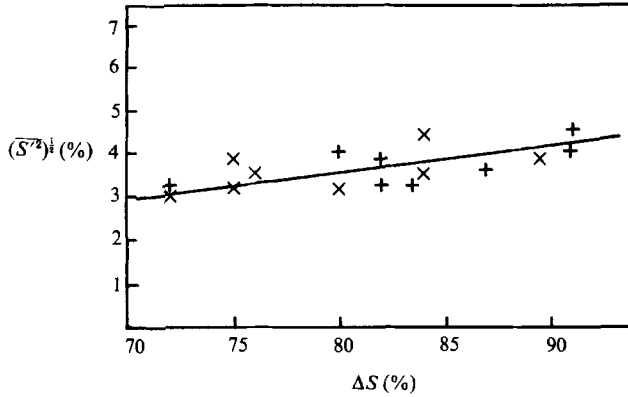
FIGURE 26. Variation of r.m.s. salinity fluctuations within the salt interfacial layer $(\overline{S'^2})^{\frac{1}{2}}$ with the salinity difference ΔS during the low-stability regime.
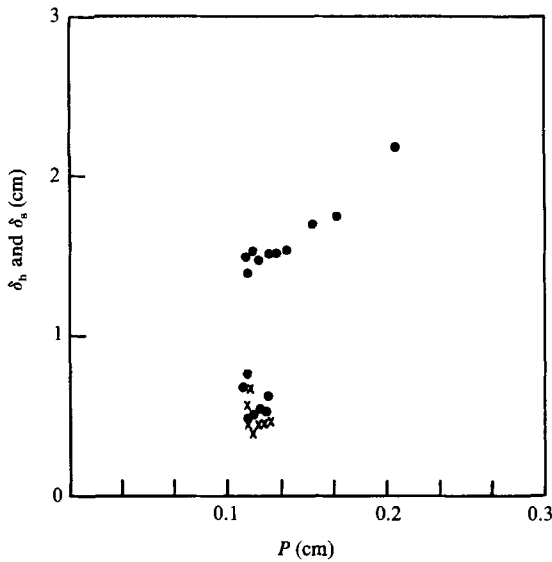
FIGURE 27. Measurement of the interfacial-layer thicknesses during the low-stability regime: ●, heat; ×, salt. The heat interfacial-layer thickness variation during the diffusive regime is also plotted (upper ● symbols) to illustrate the reduction of the thickness with the initiation of the low-stability regime.

proportionality constants 0.047 and 0.043, respectively. Also from figure 27, a substantial decrease of δ_s and δ_h with the onset of the low-stability regime is noted. At subsequent times, $t > t_b$, the interfacial-layer thicknesses were found to adjust in such a way that $\delta_s \approx \delta_h$.

7.3. *Transport of heat and salt*

The role of turbulent eddies in enhancing the heat and salt transfer across an interface has already been discussed. Based on the assumption that, at low stabilities, a significant amount of heat and mass exchange occurs by direct contact between the eddies, the turbulent salt and heat fluxes may be parameterized as $\overline{S'w'} \sim (\overline{S'^2})^{\frac{1}{2}}(\overline{w'^2})^{\frac{1}{2}} \sim \Delta S u_*$, and $\overline{T'w'} \sim (\overline{T'^2})^{\frac{1}{2}}(\overline{w'^2})^{\frac{1}{2}} \sim \Delta T u_*$, where w' is the fluctuating vertical velocity just below the interface. Following Linden (1974), the diffusive flux
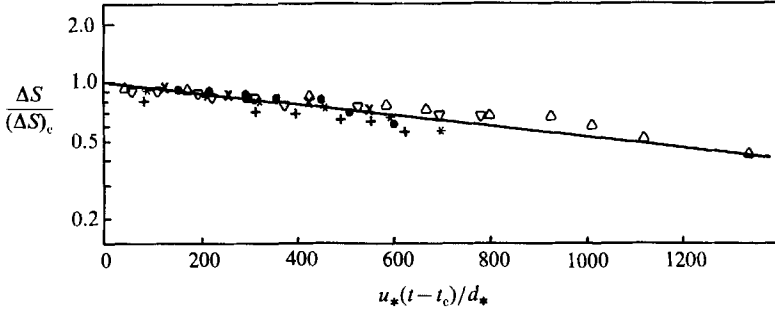
FIGURE 28. A semi-log plot of $\Delta S/\Delta S_c$ vs. $u_*(t-t_c)/d_*$. Subscript c denotes the conditions corresponding to the onset of the low-stability regime. The symbols have the same meaning as in figure 10.
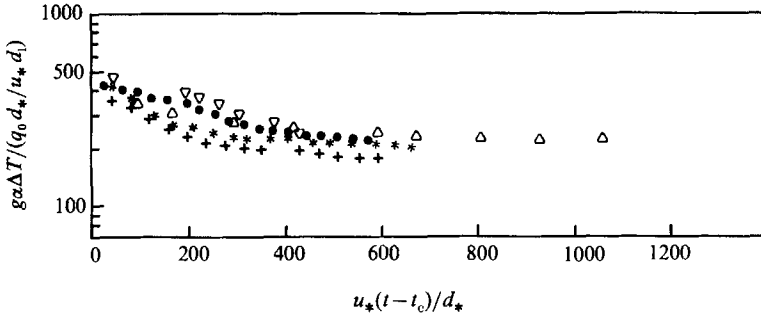

FIGURE 29. A semi-log plot of $g\alpha\Delta T/(q_0 d_*/d_1 u_*)$ vs. $u_*(t-t_c)/d_*$. The symbols have the same meaning as in figure 10.

contribution may also be written in the same form and, hence, the *total* salt and heat fluxes can be written as

$$g\beta F_s = k_1(g\beta\Delta S)\,u_*, \quad g\alpha F_h = k_2(g\alpha\Delta T)\,u_*. \qquad (41\,a,\,b)$$

Thus using (18) and (19),

$$-\frac{\mathrm{d}(g\beta\Delta S)}{\mathrm{d}t} = \frac{k_1\,g\beta\Delta S u_*}{d_*}, \qquad (42\,a)$$

$$\frac{\mathrm{d}(g\alpha\Delta T)}{\mathrm{d}t} + k_2\,g\alpha\Delta T\frac{u_*}{d_*} = \frac{q_0}{d_1}. \qquad (42\,b)$$

Assuming that the d_* and d_1 variation with time is small compared to the ΔT and ΔS variation (which is confirmed by experiments (Huppert 1971)), solutions for (42 a, b) are

$$\frac{\Delta S}{\Delta S_c} = \exp\left[-k_1\frac{u_*}{d_*}(t-t_c)\right] \qquad (43\,a)$$

and

$$\frac{g\alpha\Delta T}{q_0\,d_*/k_2\,d_1\,u_*} = \left(\frac{k_2\,g\alpha\Delta T_c\,d_1\,u_*}{q_0\,d_*}-1\right)\exp\left[\frac{-k_2\,u_*(t-t_c)}{d_*}\right]+1, \qquad (43\,b)$$

where subscript c corresponds to conditions at the onset of the low-stability regime. Figures 28 and 29 show $\Delta S/\Delta S_c$ vs. $u_*(t-t_c)/d_*$ and $g\alpha\Delta T/(q_0 d_*/d_1 u_*)$ vs. $u_*(t-t_c)/d_*$ as obtained from the experimental data. The agreement is fair. The constants k_1 and k_2 can be estimated as $k_1 \approx 6.7\times 10^{-4}$ and $k_2 \approx 4.5\times 10^{-3}$ so that $k_1/k_2 \approx 0.15$. The results of the direct flux measurements (§4) are also shown, in figures 30–32. These
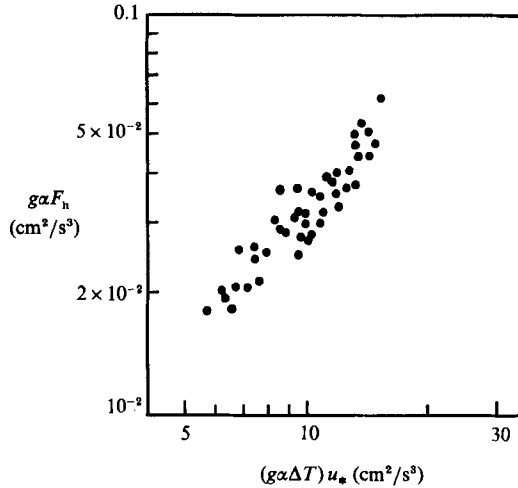
FIGURE 30. Variation of measured heat flux $g\alpha F_h$ with $(g\alpha\Delta T)\,u_*$ in the low-stability regime.
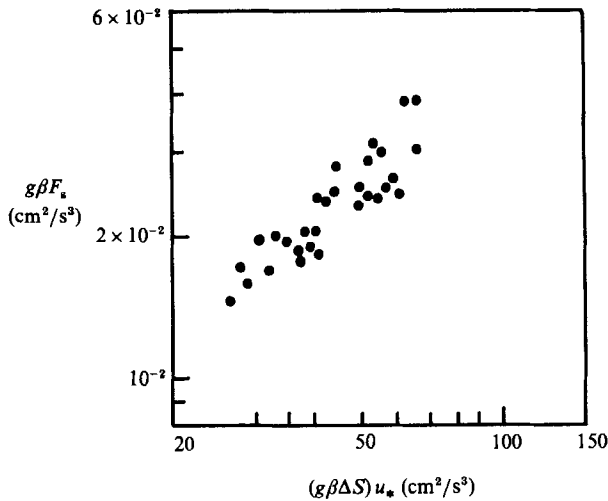

FIGURE 31. Variation of measured salt flux $g\beta F_s$ with $(g\beta\Delta S)\,u_*$ in the low-stability regime.

measurements, although they show considerable scatter, support flux laws of the form in 41 (a, b) and suggest that $k_1 \approx 5.5 \times 10^{-4}$ and $k_2 \approx 3.4 \times 10^{-3}$, which are not inconsistent with the above values.

The scatter of the data may be due, in part, to the entrainment at the interface, which gives rise to an additional buoyancy flux. Differential turbulence levels across the interface cause it to migrate upwards and the rate of entrainment is a decreasing function of the interfacial Richardson number. Since low R_ρ is usually associated with low Richardson numbers, we may expect the scatter to increase with decreasing R_ρ. Moreover, the buoyancy flux depends on both R_ρ and Ri for small R_ρ. In the present experiments, flux measurements were not taken when the interfacial migration appeared to be substantial. Figure 32 also shows the measurements of Turner (1965), and more recent data of Taylor (1988), who reported the values of R_F at very low R_ρ. While Turner's data appear to be at odds with the present results, the
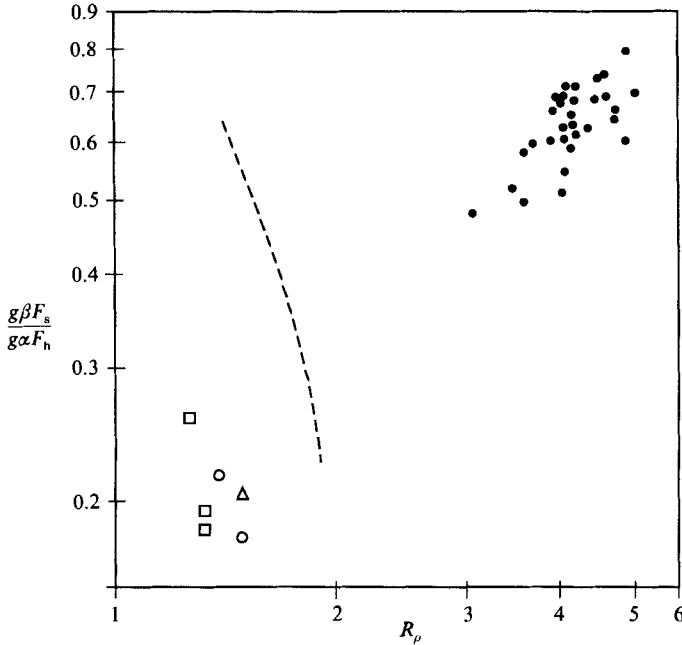
FIGURE 32. Variation of $R_{\rm F} = g\beta F_{\rm s}/g\alpha F_{\rm h}$ with R_ρ in the low-stability regime. ●, present data; □, ○, △, data of Taylor (1988) at $R_\rho < 1.9$; —--, Turner's (1965) data.

data of Taylor (1988) seem to be in general agreement with the proposed flux law (41) for the low-stability regime.

8. Entrainment

The migration of the density interface was a noticeable feature at low R_ρ (§5). Since the convection in the lower layer is stronger than that in the upper layer, the differential turbulence levels across the interface cause it to migrate upwards while manifesting net entrainment from the upper layer. The interfacial position was monitored with time, and the time (§4) where the interface starts migrating was estimated. Figure 33 shows Δb vs. u_*^2/l_1, where $l_1 \approx 0.25d_1$, evaluated at this time. The results show that the interfacial migration starts when the Richardson number $Ri \approx \Delta b l_1/u_*^2$ falls below a critical value $Ri_{\rm v} \approx 34$. According to the flow visualization studies, the entrainment occurs by the impinging eddies on the interfacial layer that scour and detach thin elements of fluid from it; such elements are eroded and homogenized with the rest of the fluid by the mixed-layer turbulence. In the case of mechanically generated shear-free entrainment experiments, the predominant mixing mechanism is the interfacial wave breaking (Fernando & Long 1983; Hannoun & List 1988). In the present experiments no such events were observed. Perhaps the diffusive nature of the interface may have suppressed the growth of such waves (Crapper & Linden 1974; Pearson & Linden 1983).

Eddies of integral scales can engulf fluid across density interfaces, as in an unstratified fluid, when the Richardson number Ri is less than about 2 (Turner 1973) but the observations made by Fernando & Long (1985) indicate that even when $Ri > 2$, large-scale eddies are involved in the entrainment by impinging on the density interface and splashing the fluid into the mixed layer. When $Ri > 30$, this mechanism
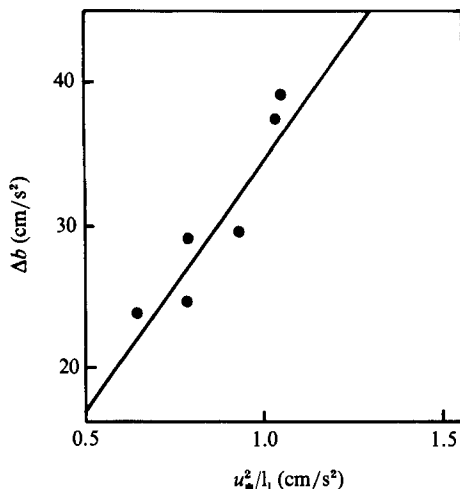
FIGURE 33. Variation of Δb with u_*^2/l_1 evaluated at the beginning of the interfacial migration.

becomes completely inoperative, the eddies tend to flatten at the density interface (Long 1978; Hannoun, Fernando & List 1988) and wave breaking is the predominant mixing mechanism. Based on these observations, it is possible to argue that, when $Ri > 30$, a significant entrainment may not be observable in the present experiments owing to the absence of interfacial waves, but as Ri drops below this critical value, the scouring of the interfacial layer by the energy-containing eddies can cause entrainment. However, unlike the behaviour for $Ri < 2$, in this case, u_e/u_* is dependent on Ri. A detailed investigation, using eddy break-up devices, on the involvement of large-scale eddies during entrainment in thermohaline systems has been performed; the results will be presented elsewhere. Another important point to note is that, in thermohaline convection, the entrainment need not be associated with Rayleigh–Taylor instability that leads to the condition $\alpha\Delta T = \beta\Delta S$ at the interface, but can occur due to mechanical entrainment by the mixed-layer eddies (cf. Turner 1968).

9. Discussion

In the preceding sections, a detailed account of the theoretical analysis and the experimental results pertaining to the heat and salt transfer across a diffusive interface were presented. The important features of this work are summarized here.

(a) Bottom heating of a two-fluid system, consisting of a freshwater layer overlying a saline layer, leads to turbulent convection in both layers. The heat transfer to the upper layer occurs through an interfacial layer which is purely diffusive. It was argued that the diffusive interface should have a double boundary-layer structure, in which the salt interfacial layer is much thinner than the heat interfacial layer. This suggestion was also examined experimentally.

(b) A simple theory was presented to predict heat and salt fluxes across the interface and the time dependency of temperature and salinity in the convecting layers when the bottom heat flux is constant. Within a certain time period the theoretical predictions were in good agreement with the experiment, but then exhibited a complete departure. Measurements and qualitative observations suggest

that the observed deviation may be due to the onset of a 'low-stability' buoyancy transfer regime, in which the distortion of the salt interface and physical contact between the upper- and lower-layer turbulent eddies are dominant features. A criterion, based on energy arguments, was derived to predict the initiation of the low-stability regime and was verified experimentally.

(c) The onset of low-stability transport was associated with a considerable increase in heat and salt fluxes. With the onset, the heat and salt interfacial-layer thicknesses decreased appreciably and the presence of the double boundary-layer structure was not evident. Under these conditions, r.m.s. salinity and temperature fluctuation measurements were also made within the interfacial layer.

(d) When the overall Richardson number of the interface falls below a critical value Ri_v, an upward migration of the interface could be observed. Usually this movement was encountered during the low-stability transport regime. Estimates show that Ri_v is comparable with a previously reported critical Richardson number, above which the large eddies of the size of the integral lengthscale flatten at the density interface without being directly involved in the entrainment process.

An interpretation of some geophysical observations in the light of the present experimental results will now be attempted. Newman (1976) has made extensive measurements in Lake Kivu, an East African rift lake, with a single outflow. A step-like microstructure containing convecting layers separated by diffusive interfaces has been observed at mid-depths of the lake and bottom geothermal springs are believed to be responsible for supplying the bottom heat flux. The observed parameters (at station D1) are $q_h \approx 4 \times 10^{-10}$ m^2 s^{-3}, $q_s \approx 1.2 \times 10^{-10}$ m^2 s^{-3}, $g\alpha\Delta T \approx 7.1 \times 10^{-5}$ m s^{-2}, $g\beta\Delta S \approx 1.4 \times 10^{-4}$ m s^{-2} and $d_u \approx 1.4$ m. For this case, the diffusive heat flux calculated using 12(b) is 4.0×10^{-11} m^2 s^{-3}, which is much smaller than the observed value. However, if R and $C_2(q_0 d_1)^{\frac{2}{3}}$ which appear in (40a) are calculated for this region, the values 1.1×10^{-7} and 1.5×10^{-7} m^2 s^{-2}, respectively, are obtained, suggesting the possibility of low-stability transport. Hence, (41a, b) may be used to calculate the heat and salt fluxes as $q_h \approx 3.5 \times 10^{-10}$ m^2 s^{-3} and $q_s \approx 1.0 \times 10^{-10}$ m^2 s^{-3}, which are in good agreement with the observed values.

It is known that the Bering Sea, that separates the Arctic and Pacific oceans, plays a significant role in the general circulation of the ocean. Oceanographic data obtained from the central Bering Sea Marginal Ice Zone by Stegan, Hendricks & Muench (1985) (see also Hendricks, Muench & Stegan 1985; Kantha 1986), indicate that water passing through the Bering Sea can be significantly modified by the air–sea interaction process. During May to November the region is ice free, but in November ice is formed in the north Bering Sea by cold north-easterly winds. The ice is advected southwards and is replaced by newly formed ice. The ice cover continues to expand until February–March, where it reaches its most southernly extent near the shelf break, and remains there for a couple of months with the ice input from the north locally balanced by melting ice, thus maintaining a quasi-stationary state. Two layers, separated by a density interface of diffusive nature, are quite discernible under the ice cover, but towards the ice edge, the vertical structure tends to be more homogenous, indicating enhanced mixing. The gradient Richardson number in this region has been found to be about 4, thus excluding the possibility of mixing due to shear instabilities. The typical values obtained from figure 2 of Stegan et al. (1985) are $g\alpha\Delta T \approx 5.9 \times 10^{-4}$ m s^{-2}, $R_\rho = 4$, $d_u = 35$ m, $d_1 = 20$ m, and $\alpha \approx 6.5 \times 10^{-5}$ K^{-1} is reasonable. The heat supply rate, based on the drift velocity and frontal width of the ice zone, is $Q \approx 180$ W m^{-2}, corresponding to $q_0 \approx 2.6 \times 10^{-8}$ m^2 s^{-3}. The quantities of (40a) may be calculated as $R \approx 6.7 \times 10^{-6}$ m^2 s^{-2} and $C_2(q_0 d_1)^{\frac{2}{3}} \approx 10^{-5}$ m^2 s^{-2},

indicating the manifestation of low-stability transport. Using (41*a*), it is possible to evaluate the associated heat flux as $q_0 \approx 3 \times 10^{-8}$ m² s⁻³ (or $Q \approx 207$ W m⁻²), which is consistent with the observed value. The accompanying salt flux can be also predicted, using (41*b*), as 1.9×10^{-8} m² s⁻³ or 1.9×10^{-10} kg m⁻² s.

From the preceding discussion it appears that, although there are differences between the laboratory and oceanic conditions, the laboratory experiments are capable of making satisfactory predictions for certain oceanic phenomena. In recent years a large number of oceanic observations have been made on diffusive interfaces and the application of the present results to such cases will be addressed in a separate paper (Fernando 1989).

REFERENCES

ADRIAN, R. J., FERREIRA, R. T. D. & BOBERG, T. 1986 Turbulent convection in wide horizontal layers. *Expts Fluids* **4**, 121.

CRAPPER, P. F. 1975 Measurements across a diffusive interface. *Deep-Sea Res.* **22**, 537.

CRAPPER, P. F. & LINDEN, P. F. 1974 The structure of the turbulent density interfaces. *J. Fluid Mech.* **65**, 45.

DEGENS, E. T. & ROSS, D. A. 1969 *Hot Brines and Recent Heavy Metal Deposits in the Red Sea.* Springer.

FERNANDO, H. J. S. 1989 Oceanographic implications of laboratory experiments on diffusive interfaces. *J. Phys. Oceanogr.* (in Press.)

FERNANDO, H. J. S. & LONG, R. R. 1983 The growth of a grid-generated turbulent mixed layer in a two-fluid system. *J. Fluid Mech.* **133**, 377.

FERNANDO, H. J. S. & LONG, R. R. 1985 On the nature of the entrainment interface of a two-layer fluid subjected to zero-mean-shear turbulence. *J. Fluid Mech.* **151**, 21.

FOSTER, T. D. & CARMACK, E. C. 1976 Temperature and salinity structure in the Weddell Sea. *J. Phys. Oceanogr.* **6**, 36.

GREGG, M. C. & COX, C. S. 1972 The vertical microstructure of temperature and salinity. *Deep-Sea Res.* **19**, 355.

GRIFFITHS, R. W. 1979 The transport of multiple components through thermohaline diffusive interfaces. *Deep-Sea Res.* **26**, 383.

HANNOUN, I. A., FERNANDO, H. J. S. & LIST, E. J. 1988 Turbulence structure near a sharp density interface. *J. Fluid Mech.* **189**, 189.

HANNOUN, I. A. & LIST, E. J. 1988 Turbulent mixing at a shear-free density interface. *J. Fluid Mech.* **189**, 211.

HENDRICKS, P. J., MUENCH, R. D. & STEGAN, G. R. 1985 A heat balance for the Bering Sea Ice Edge. *J. Phys. Oceanogr.* **15**, 1747.

HOARE, R. A. 1966 Problems of heat transfer in Lake Vanda, a density stratified Arctic lake. *Nature* **210**, 787.

HOARE, R. A. 1968 Thermohaline convection in Lake Vanda, Antarctica. *J. Geophys. Res.* **73**, 607.

HUNT, J. C. R. 1983 Turbulence structure and turbulent diffusion near gas–liquid interface. In *Proc. Intl Symp. on Gas Transfer across Water Surfaces, Ithaca, N.Y.* (ed. W. Brutsaert & G. H. Jirka).

HUNT, J. C. R. 1984 Turbulence structure in thermal convection and shear-free boundary layers. *J. Fluid Mech.* **138**, 161.

HUPPERT, H. E. 1971 On the stability of a series of double diffusive layers. *Deep-Sea Res.* **18**, 1005.

HUPPERT, H. E. & TURNER, J. S. 1972 Double diffusive convection and its implications for the temperature and salinity structure of the ocean and Lake Vanda. *J. Phys. Oceanogr.* **2**, 456.

HUPPERT, H. E. & TURNER, J. S. 1981 Double-diffusive convection. *J. Fluid Mech.* **106**, 299.

KANTHA, L. H. 1986 Comments on 'A heat balance for the Bering Sea Ice Edge'. *J. Phys. Oceanogr.* **16**, 2205.

LINDEN, P. F. 1974 A note on the transport across a diffusive interface. *Deep-Sea Res.* **21**, 283.

LINDEN, P. F. & SHIRTCLIFFE, T. G. L. 1978 The diffusive interface in double-diffusive convection. *J. Fluid Mech.* **87**, 417 (referred to as LS).

LONG, R. R. 1978 A theory of mixing in stably stratified fluids. *J. Fluid Mech.* **84**, 113.

MARMORINO, G. O. & CALDWELL, D. R. 1976 Heat and salt transport through a diffusive thermohaline interface. *Deep-Sea Res.* **23**, 59.

MUNNS, R. G., STANLEY, R. J. & DENSMORE, C. D. 1967 Hydrographic observations of the Red Sea brines. *Nature* **214**, 1215.

NARUSAWA, V. 1986 Structure of diffusive interface of double diffusive convection. *ASME paper* 86-HT-3.

NEAL, V. T., NESHYBA, S. & DENNER, W. 1969 Thermal stratification in the Arctic Ocean. *Science* **166**, 373.

NESHYBA, S., NEAL, V. T. & DENNER, W. 1971 Temperature and conductivity measurements under Ice Island T-3. *J. Geophys. Res.* **76**, 8107.

NEWELL, T. A. 1984 Characteristics of double-diffusive interface at high density-stability ratios. *J. Fluid Mech.* **149**, 385.

NEWMAN, F. C. 1976 Temperature steps in Lake Kivu: a bottom heated saline lake. *J. Phys. Oceanogr.* **6**, 157.

PEARSON, H. & LINDEN, P. F. 1983 The final state of decay of turbulence in stably stratified fluid. *J. Fluid Mech.* **134**, 195.

SHIRTCLIFFE, T. G. L. 1973 Transport and profile measurements of the diffusive interface in double diffusive convection with similar diffusivities. *J. Fluid Mech.* **57**, 27.

SHIRTCLIFFE, T. G. L. & CALHAEM, I. M. 1968 Measurements of temperature and electrical conductivity in Lake Vanda, Victoria Land, Antarctica. *N. Z. J. Geol. Geophys.* **11**, 976.

SPARROW, E. M., HUSAR, R. B. & GOLDSTEIN, R. J. 1970 Observations and other characteristics of thermals. *J. Fluid Mech.* **41**, 793.

STEGAN, G. R., HENDRICKS, P. J. & MUENCH, R. D. 1985 Vertical Mixing on the Bering Sea shelf. In *The Ocean Surface Wave Breaking, Turbulent Mixing and Radio Probing* (ed. Y. Toba & H. Mitsuyasu), p. 547. Reidel.

STERN, M. E. 1982 Inequalities and variational principles in double diffusive turbulence. *J. Fluid Mech.* **114**, 105.

SWALLOW, J. C. & CREASE, J. 1965 Hot salty water at the bottom of the Red Sea. *Nature* **205**, 165.

TAKAO, S. & NARUSAWA, V. 1980 An experimental study of heat and mass transfer across a diffusive interface. *Intl J. Heat Mass Transfer* **23**, 1283.

TAYLOR, J. 1988 The fluxes across a diffusive interface at low values of the density ratios. *Deep-Sea Res.* **35**, 555.

TURNER, J. S. 1965 The coupled turbulent transports of salt and heat across a sharp density interface. *Intl J. Heat Mass Transfer* **8**, 759.

TURNER, J. S. 1968 The behaviour of a salinity gradient heated from below. *J. Fluid Mech.* **33**, 183.

TURNER, J. S. 1973 *Buoyancy Effects in Fluids*. Cambridge University Press.

TURNER, J. S. 1974 Double diffusive phenomena. *Ann. Rev. Fluid Mech.* **6**, 37.

TURNER, J. S. 1985 Multicomponent convection. *Ann. Rev. Fluid Mech.* **17**, 11.

TURNER, J. S., SHIRTCLIFFE, T. G. L. & BREWER, P. G. 1970 Elemental variations of transport coefficients across density interfaces in multiple-diffusive systems. *Nature* **228**, 1083.

TURNER, J. S. & STOMMEL, H. 1964 A new case of convection in the presence of combined vertical salinity and temperature gradients. *Proc. Natl Acad. Sci.* **52**, 49.

VERONIS, G. 1968 Effect of stabilizing gradient of solute on thermal convection. *J. Fluid Mech.* **34**, 315.